



# Modified-pollen confined hybrid system: A promising union for visible-light-driven photocatalytic antibiotic degradation

Zhiqian Zhang<sup>a,1</sup>, Jianli Liang<sup>b,1</sup>, Wei Zhang<sup>a</sup>, Min Zhou<sup>a</sup>, Xianglin Zhu<sup>a</sup>, Zheyang Liu<sup>a</sup>, Yang Li<sup>b</sup>, Zhiqiang Guan<sup>b</sup>, Chun-Sing Lee<sup>b</sup>, Po Keung Wong<sup>c,d</sup>, Huaming Li<sup>a,\*</sup>, Zhifeng Jiang<sup>a,\*</sup>

<sup>a</sup> Institute for Energy Research, Jiangsu University, Zhenjiang 212013, China

<sup>b</sup> Center of Super-Diamond and Advanced Films (COSDAF), Department of Chemistry, City University of Hong Kong, Hong Kong Special Administrative Region of China

<sup>c</sup> School of Life Sciences, The Chinese University of Hong Kong, Shatin, NT 999077, Hong Kong Special Administrative Region of China

<sup>d</sup> Institute of Environmental Health and Pollution Control, School of Environmental Science & Engineering, Guangdong University of Technology, Guangzhou 510006, China

## ARTICLE INFO

### Keywords:

Natural-based material

Cu<sub>2</sub>O

Photocatalytic

Antibiotics removal

## ABSTRACT

The construction of catalysts with high efficiency of charge separation and high stability is of great significance for the photodegradation of organic pollutants. Herein, an eco-friendly and highly efficient three-dimensional biohybrid photocatalyst, carbonized rape pollen confined Cu<sub>2</sub>O nanoparticles (Cu<sub>2</sub>O/BC), was fabricated for the photodegradation of tetracycline under visible-light illumination. The Cu<sub>2</sub>O/BC exhibits excellent photocatalytic activity towards the degradation of tetracycline under visible-light irradiation, the degradation rate is roughly 6.0 and 3.2 times higher than BC and Cu<sub>2</sub>O. The enhanced performance is attributed to the construction of heterojunction, which promotes the effective separation of photogenerated carriers. In addition, the three-dimensional hollow BC with spatial domain confinement ensures the structural stability of Cu<sub>2</sub>O. This work provides crucial insights into the utilization of nature-based biological materials in biohybrid photocatalysis for efficient antibiotic removal and environmental remediation.

## 1. Introduction

Antibiotics have been extensively used in humans and veterinarians for their excellent performance to treat bacterial infections [1]. However, the production and misuse of antibiotics have led to the discharge of large amounts of antibiotic wastewater into the environment [2]. Although the concentration of antibiotic residues in water systems is still low, it has the potential to cause negative environmental effects, such as antibiotic resistance to bacteria, disruption to ecosystems, and possible risks to human health [3–5]. Many effective and economical techniques have been developed for the elimination of antibiotics from water and wastewater, including adsorption [6], microbial degradation [7], electrolysis [8], photocatalysis [9], and membrane separation [10]. Among them, photocatalysis has attracted numerous attention due to its advantages such as being environment-friendly, cost-effective, and high-efficiency [11]. However, the photocatalytic performance depends on the photocatalyst to a great extent, it is quite essential to design a low-cost and efficient photocatalytic material.

Cuprous oxide (Cu<sub>2</sub>O), a familiar and typical p-type semiconductor with a narrow band gap, is considered a promising candidate in photocatalytic fields [12]. Moreover, Cu<sub>2</sub>O is abundant, inexpensive, and environmentally friendly [13,14]. Although Cu<sub>2</sub>O has the potential to become an ideal catalyst for the photocatalytic reaction, it is limited by photoelectron and hole separation, transport capabilities, and poor light stability due to self-light corrosion [15,16]. Meanwhile, Cu<sub>2</sub>O tends to agglomerate which is unfavorable to the exposure of reactive sites. Therefore, it is a thorny problem to improve its photocatalytic performance, dispersity, and stability, simultaneously. Many strategies such as doping [17], structure engineering [18], exposed facet engineering [19], and semiconductor compositing [20], etc. have been applied to solve the above problems. Among these methods, anchoring Cu<sub>2</sub>O on a suitable semiconductor material is one of the most effective methods to prevent electron-hole recombination and improve dispersity, photostability, and photocatalytic efficiency.

Biomass-derived materials with multiple scales and hierarchical morphologies have attracted extensive attention from researchers. It has

\* Corresponding authors.

E-mail addresses: [lihm@ujs.edu.cn](mailto:lihm@ujs.edu.cn) (H. Li), [jiangzf@ujs.edu.cn](mailto:jiangzf@ujs.edu.cn) (Z. Jiang).

<sup>1</sup> These authors contributed equally to this work.

been reported that rape pollen showed large pore volumes, high surface areas, and a 3D porous network structure with a uniform carbon skeleton [21,22]. The unique structure of treated rape pollen can not only better disperses Cu<sub>2</sub>O particles to inhibit their self-aggregation, but also promotes the separation of the photogenerated holes and electrons by decreasing diffusion length from bulk to surface [23]. In addition, treated rape pollen contains heteroatomic nitrogen that may confer semiconductor-like properties [21,24–26], allowing for electron conduction between it and Cu<sub>2</sub>O and constructing a heterogeneous structure. More importantly, rape pollen is widely available, cost-effective, and biocompatible [27], which overcoming the disadvantages of traditional carbon-based photocatalysts prepared by complicated procedures with expensive chemical precursors.

Herein, a three-dimensional carbonized rape pollen confined Cu<sub>2</sub>O nanoparticles photocatalyst (Cu<sub>2</sub>O/BC) is successfully prepared by a facile and economic strategy. The performance of Cu<sub>2</sub>O/BC is 6.0 times and 3.2 times higher than that of BC and Cu<sub>2</sub>O particles, respectively. The Cu<sub>2</sub>O/BC photocatalyst is suitable for a wide range of temperatures and pH, as well as the presence of a variety of inorganic ions and organic substance (HA), revealing its application potential. The degradation results from simulated solar sources also indicate that Cu<sub>2</sub>O/BC has a wide spectral absorption range and is appropriate for practical application. Meanwhile, the degradation efficiency for tap water, agricultural wastewater, industrial wastewater, and rainwater reached 64%, 49%, 49%, and 42%, respectively, indicating a great potential in wastewater treatment. The active species of photodegradation were systematically investigated by ROS trapping experiments and electron spin resonance (ESR). In addition, the degradation pathways of TC were analyzed by liquid chromatography-mass spectrometry (LC-MS) and density functional theory calculation (DFT). The transformation processes of TC and the toxicity of intermediates were studied by three-dimensional excitation and emission matrix fluorescence spectroscopy (3D EMMs) and antibacterial experiments (against *E. coli* and *R. rubrum*). The work suggests that the natural pollen-based photosensitization process is promising for effective antibiotic treatment, which assists in real water purification.

## 2. Experimental section

### 2.1. Materials

The rape pollen used in this study was purchased from a food processing factory (Wang's Food, Jiangsu, China) on Taobao.com. Anhydrous ethanol (C<sub>2</sub>H<sub>5</sub>OH), sulfuric acid (H<sub>2</sub>SO<sub>4</sub>), copper chloride dehydrate (CuCl<sub>2</sub>·0.2 H<sub>2</sub>O), sodium hydroxide (NaOH), ascorbic acid (C<sub>6</sub>H<sub>8</sub>O<sub>6</sub>), cetyl trimethyl ammonium bromide (C<sub>19</sub>H<sub>42</sub>BrN) and tetracycline (TC) were purchased from Sinopharm Chemical Reagent Co. Ltd (Shanghai, China). All chemicals were from commercial sources and used without any further purification. Deionized water was used in all the experiments.

### 2.2. Synthesis of photocatalysts

#### 2.2.1. Synthesis of BC

Firstly, 10 g of commercial rape pollen (RP) was dispersed in anhydrous ethanol (250 mL), sonicated for 4 h, and then filtered and washed several times. After that, it was added to H<sub>2</sub>SO<sub>4</sub> (100 mL, 4 M) solution and stirred in an oil bath for 4 h, then washed several times with water. Subsequently, the samples were heated to 350 °C at a rate of 2 °C per minute in a high-purity nitrogen atmosphere for 2 h. Finally, the samples were sonicated with ethanol for 30 min and washed several times with water. After drying in a vacuum for 6 h, BC catalysts were obtained.

#### 2.2.2. Synthesis of Cu<sub>2</sub>O/BC

Firstly, 0.1 g BC and 0.2 g cetyltrimethylammonium bromide (CTAB) were dispersed in 100 mL deionized water for 1 h with sonication and

stirring for 30 min. Then 4.2 mL CuCl<sub>2</sub>·0.2 H<sub>2</sub>O solution (0.1 M) was added dropwise to the above solution and stirred for 1 h. After adding 10 mL of NaOH solution (0.2 M) and further stirring for 30 min, 10 mL of ascorbic acid solution (0.1 M) was added dropwise to the suspension and stirred for 5 min. The mixture was washed three times with water, three times with alcohol, and dried under vacuum for 6 h to obtain Cu<sub>2</sub>O/BC catalysts.

#### 2.2.3. Synthesis of BC-Cu<sub>2</sub>O

BC-Cu<sub>2</sub>O photocatalysts were prepared by mechanically mixing and stirring certain amount of BC and Cu<sub>2</sub>O products.

### 2.3. Photoelectrochemical measurements

CHI 660E electrochemical workstation and high uniformity integrated xenon light source (PLS-FX300HU, Beijing Perfectlight) were used to test the photocurrent response and electrochemical impedance spectroscopy (EIS). In detail, 5 mg of the photocatalyst was dispersed in 980 µL of isopropanol and 20 µL of Nafion, then the dispersed mixture was dip-coated onto the ITO substrate (1 × 1 cm<sup>2</sup>) for testing. The electrochemical test was performed in a 3-electrode configuration with the assembled photoelectrodes (photocatalyst on ITO glass) as the working electrode, the Pt slice as the counter electrode, and the Ag/AgCl as the reference electrode, and 0.2 M Na<sub>2</sub>SO<sub>4</sub> solution was used as electrolyte.

### 2.4. Photocatalytic performance evaluation

In a typical experiment, 30 mg photocatalyst was added into 50 mL 20 mg L<sup>-1</sup> TC aqueous solution, and the adsorption-desorption equilibrium was achieved by continuous magnetic stirring for 60 min in the dark. The outer and inner walls of the photoreactor are made of quartz, with an inner wall height of 15 cm, a diameter of 4.5 cm, and an inner volume of 250 mL. The visible light was simulated by a 250 W xenon lamp equipped with a 400 nm cutoff filter. Under simulated visible light irradiation, 4 mL of the suspension was sampled at intervals of 30 min and filtered through a 0.22 µm filter membrane, the concentration of TC was measured by a UV-vis spectrophotometer (UV-1800, Shimadzu, Japan) by checking its maximum absorption wavelength at 357 nm. The degradation efficiency (DE, %) was calculated by the following equation:

$$DE(\%) = \frac{C_0 - C_t}{C_0} \times 100\% \quad (1)$$

Where C<sub>0</sub> is the concentration of TC after the dark reaction, and C<sub>t</sub> is the TC concentration at time t.

## 3. Results and discussion

### 3.1. Characterization of as-prepared materials

The typical fabrication process of Cu<sub>2</sub>O/BC is shown in Fig. 1a (detailed synthesis as shown in the Experimental section). Fig. 1c shows the XRD patterns of Cu<sub>2</sub>O/BC, BC, and Cu<sub>2</sub>O. The peaks of nanocrystalline Cu<sub>2</sub>O (JCPDS No. 05-0667) and BC were observed in the XRD pattern of Cu<sub>2</sub>O/BC, indicating that Cu<sub>2</sub>O and BC are successfully combined. Fourier transform infrared spectroscopy (FTIR) was used to further analyze the chemical structures. The peak at 2930 cm<sup>-1</sup> corresponds to the stretching vibrations of aliphatic C-H (Fig. 1b), and peaks at 1700 cm<sup>-1</sup> and 1450 cm<sup>-1</sup> are attributed to the stretching vibrations of C=O and the asymmetric bending of -CH<sub>3</sub>, respectively [28]. Notably, a sharp peak at 624 cm<sup>-1</sup> attributed to the Cu (I)-O stretching vibration can be observed in Cu<sub>2</sub>O/BC, suggesting the successful loading of Cu<sub>2</sub>O on BC [29]. Meanwhile, the zeta potential of BC, Cu<sub>2</sub>O, and Cu<sub>2</sub>O/BC were measured to be -40.2 mV, 15.3 mV, and -19.3 mV



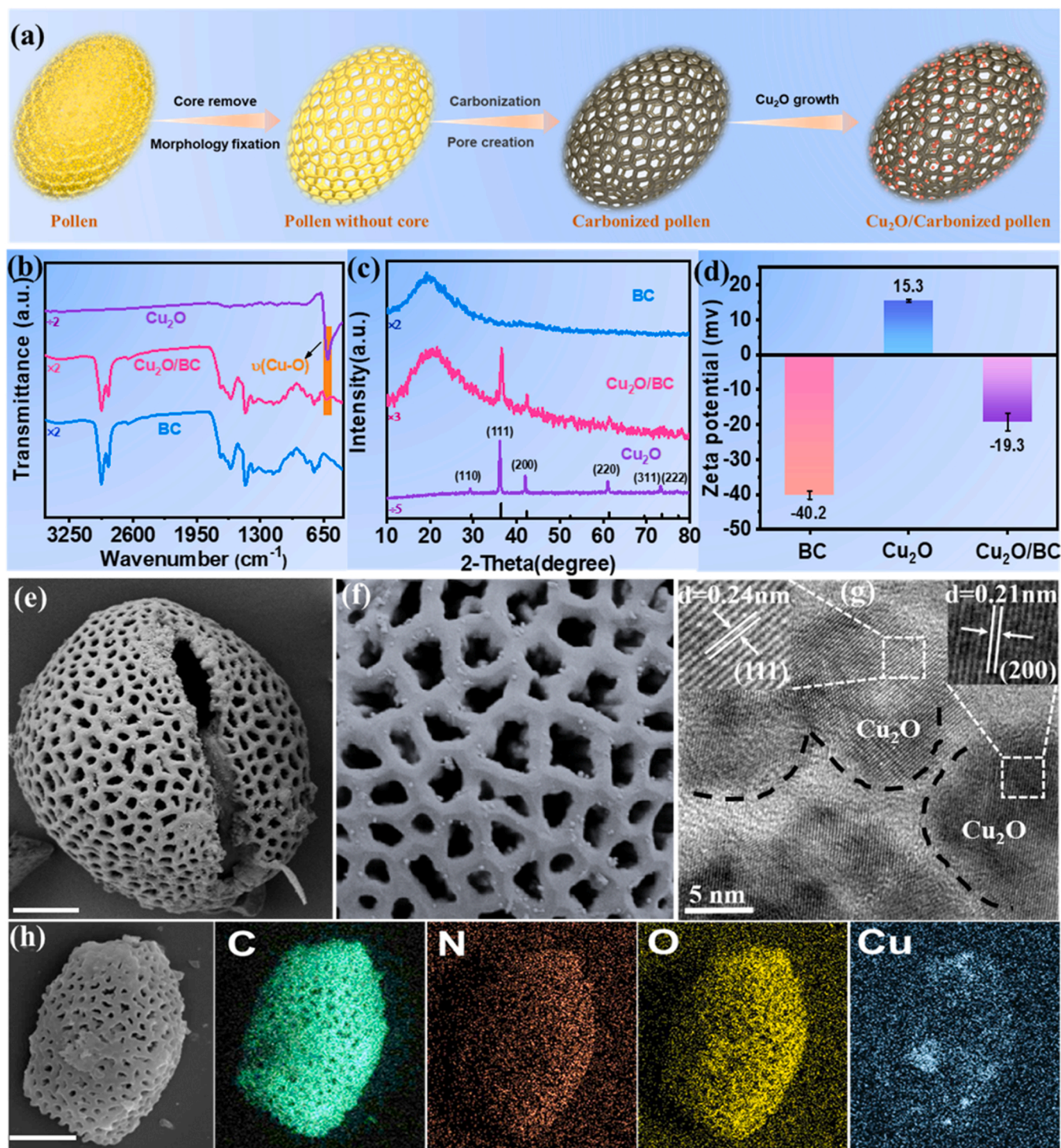


**Fig. 1.** a) Schematic diagram of  $\text{Cu}_2\text{O}/\text{BC}$  synthesis. b) FTIR spectra. c) XRD pattern and d) Zeta potential of BC,  $\text{Cu}_2\text{O}$  and  $\text{Cu}_2\text{O}/\text{BC}$ . e, f) SEM images of  $\text{Cu}_2\text{O}/\text{BC}$ . g) HRTEM image of the  $\text{Cu}_2\text{O}/\text{BC}$ . h) elemental mappings of  $\text{Cu}_2\text{O}/\text{BC}$  (C, N, O and Cu).

(Fig. 1d), respectively, manifesting a strong electrostatic attraction between BC and  $\text{Cu}_2\text{O}$ , which further illustrates the two monomers can achieve effective combination. The scanning electron microscopic (SEM) images (Fig. 1e, Fig. S2) display that the BC possesses a three-dimensional (3D) porous network structure. Importantly, the existence of well-distributed and abundant pore channels within the BC structure is beneficial to the harvest of light and absorption of pollutants [21]. As shown in Fig. 1f,  $\text{Cu}_2\text{O}$  nanoparticles are homogeneously loaded on the surface of BC, and even some  $\text{Cu}_2\text{O}$  nanoparticles are embedded

in the pore channels of BC, which can protect  $\text{Cu}_2\text{O}$  from photocorrosion. Notably, the pure  $\text{Cu}_2\text{O}$  particles are large and agglomerated (Fig. S1), which are susceptible to photocorrosion in the reaction. On the contrary, after in situ anchoring on BC, small and uniformly dispersed  $\text{Cu}_2\text{O}$  particles can be obtained due to the spatial confinement effect of BC, which is conducive to the stable existence of  $\text{Cu}_2\text{O}$ . In addition, the high-resolution TEM (HRTEM) image (Fig. 1g) shows the well-defined lattice fringes of particles within  $\text{Cu}_2\text{O}/\text{BC}$ , the interplanar space of 0.24 nm and 0.21 nm coincide with the individual plane of  $\text{Cu}_2\text{O}$  (111)

and (200), respectively, which further reveals the successful loading of  $\text{Cu}_2\text{O}$  on BC. The element mapping of  $\text{Cu}_2\text{O}/\text{BC}$  (Fig. 1h) confirms the coexistence of BC and  $\text{Cu}_2\text{O}$  and the uniform distribution of  $\text{Cu}_2\text{O}$  on BC.

The compositions and chemical states of  $\text{Cu}_2\text{O}$  and  $\text{Cu}_2\text{O}/\text{BC}$  were further investigated by X-ray photoelectron spectroscopy (XPS). The peaks at about 932.4 eV and 952.2 eV are ascribed to  $\text{Cu } 2p_{3/2}$  and  $\text{Cu } 2p_{1/2}$  of  $\text{Cu}_2\text{O}$  in  $\text{Cu}_2\text{O}/\text{BC}$  (Fig. 2a) [30], respectively, indicating the existence of  $\text{Cu}_2\text{O}$  on BC. In addition, there are low-intensity peaks at 934.5 eV and 953.9 eV attributed to  $\text{Cu}^{2+}$  of  $\text{CuO}$ , suggesting that the sample was slightly oxidized [31]. Notably, the formation of  $\text{CuO}$  can play as a protective layer on the surface of  $\text{Cu}_2\text{O}$ , which can improve the stability of  $\text{Cu}_2\text{O}$  in photocatalytic reactions [32]. The high-resolution O 1s spectra of BC (Fig. 2b) displayed two peaks at 531.8 eV and 533.5 eV, which can be attributed to  $\text{C}=\text{O}$  and  $-\text{OH}$  of BC [33], respectively. The O 1s (Fig. 2c) peak of  $\text{Cu}_2\text{O}/\text{BC}$  is divided into three overlapping peaks at 531.1 eV, 532.4 eV, and 533.1 eV. The former peak can be unequivocally attributed to lattice oxygen of  $\text{Cu}_2\text{O}$  [30], the middle might be ascribed to oxygen absorbed on the surface of  $\text{Cu}_2\text{O}/\text{BC}$  [32], and the latter is assigned to  $-\text{OH}$  of BC [34]. The above results further prove that we synthesized the  $\text{Cu}_2\text{O}/\text{BC}$  photocatalyst successfully. The specific surface area and pore volume results of the prepared samples are shown in Fig. 2b, d, the specific surface areas of  $\text{Cu}_2\text{O}/\text{BC}$  ( $5.51 \text{ m}^2 \text{ g}^{-1}$ ) and pore volume ( $0.0038 \text{ cm}^3 \text{ g}^{-1}$ ) are both higher than that of BC ( $3.45 \text{ m}^2 \text{ g}^{-1}$ ,  $0.0023 \text{ cm}^3 \text{ g}^{-1}$ ), demonstrating that the loading of  $\text{Cu}_2\text{O}$  could optimize the pore structure, which is probably beneficial to the photocatalysis reaction. The hydrophilicity of BC and  $\text{Cu}_2\text{O}/\text{BC}$  was evaluated by water contact angle (CA) measurements, respectively. As shown in Fig. 2e, f, the CA of  $\text{Cu}_2\text{O}/\text{BC}$  is  $89^\circ$ , which is lower than  $107^\circ$ , testifying that  $\text{Cu}_2\text{O}/\text{BC}$  has higher hydrophilicity, thus favoring the dispersion of the  $\text{Cu}_2\text{O}/\text{BC}$  in water and facilitating the contact between  $\text{Cu}_2\text{O}/\text{BC}$  and TC molecules [27].

### 3.2. Photocatalytic degradation performance of $\text{Cu}_2\text{O}/\text{BC}$

To evaluate the photocatalytic performance of the prepared samples, tetracycline hydrochloride (TC) was selected as a model antibiotic pollutant for degradation experiments. Before light irradiation, 60 min of dark adsorption experiment was carried out to make the adsorption-desorption equilibrium (Fig. 3a, insert picture). The photocatalytic degradation rates of BC and  $\text{Cu}_2\text{O}$  monomer were only 14% and 26% under visible light irradiation for 120 min (Fig. 3a), respectively. However, the photocatalytic removal efficiency of  $\text{Cu}_2\text{O}/\text{BC}$  was 85%, which was 6.0 and 3.2 times higher than that of BC and  $\text{Cu}_2\text{O}$  monomers, respectively. The degradation performance of BC- $\text{Cu}_2\text{O}$  was much lower than that of  $\text{Cu}_2\text{O}/\text{BC}$ , probably because the simple mechanical mixture made BC not play the role of spatial confinement, and the electron conduction between BC and  $\text{Cu}_2\text{O}$  was blocked, resulting in the ineffective separation of photogenerated electron-hole pairs, which greatly reduced the photocatalytic activity. To further quantitatively evaluate the photocatalytic activity of different photocatalysts, the kinetic curve was recorded. As shown in Fig. 3b and Fig. S5, the experimental data are in better agreement with the pseudo-first-order model, due to its higher correlation coefficients (Table S2) compared to the pseudo-second-order model. The apparent rate constants ( $k$ ) are evaluated by the following equation:

$$-kt = \ln\left(\frac{C_t}{C_0}\right) \quad (2)$$

where  $C_t$  is the TC concentration at the reaction time of  $t$  min ( $\text{mg L}^{-1}$ ),  $C_0$  is the TC concentration after dark reaction ( $\text{mg L}^{-1}$ ), and  $k$  is the apparent rate constant ( $\text{min}^{-1}$ ). It can be observed that the apparent rate constant  $k$  of  $\text{Cu}_2\text{O}/\text{BC}$  ( $0.0160 \text{ min}^{-1}$ ) reaches 12.6 times that of BC ( $0.00127 \text{ min}^{-1}$ ), 5.9 times that of  $\text{Cu}_2\text{O}$  ( $0.00274 \text{ min}^{-1}$ ) and 3 times that of BC- $\text{Cu}_2\text{O}$  ( $0.00534 \text{ min}^{-1}$ ), respectively.

To explore the recyclability and stability of the  $\text{Cu}_2\text{O}/\text{BC}$  catalyst for

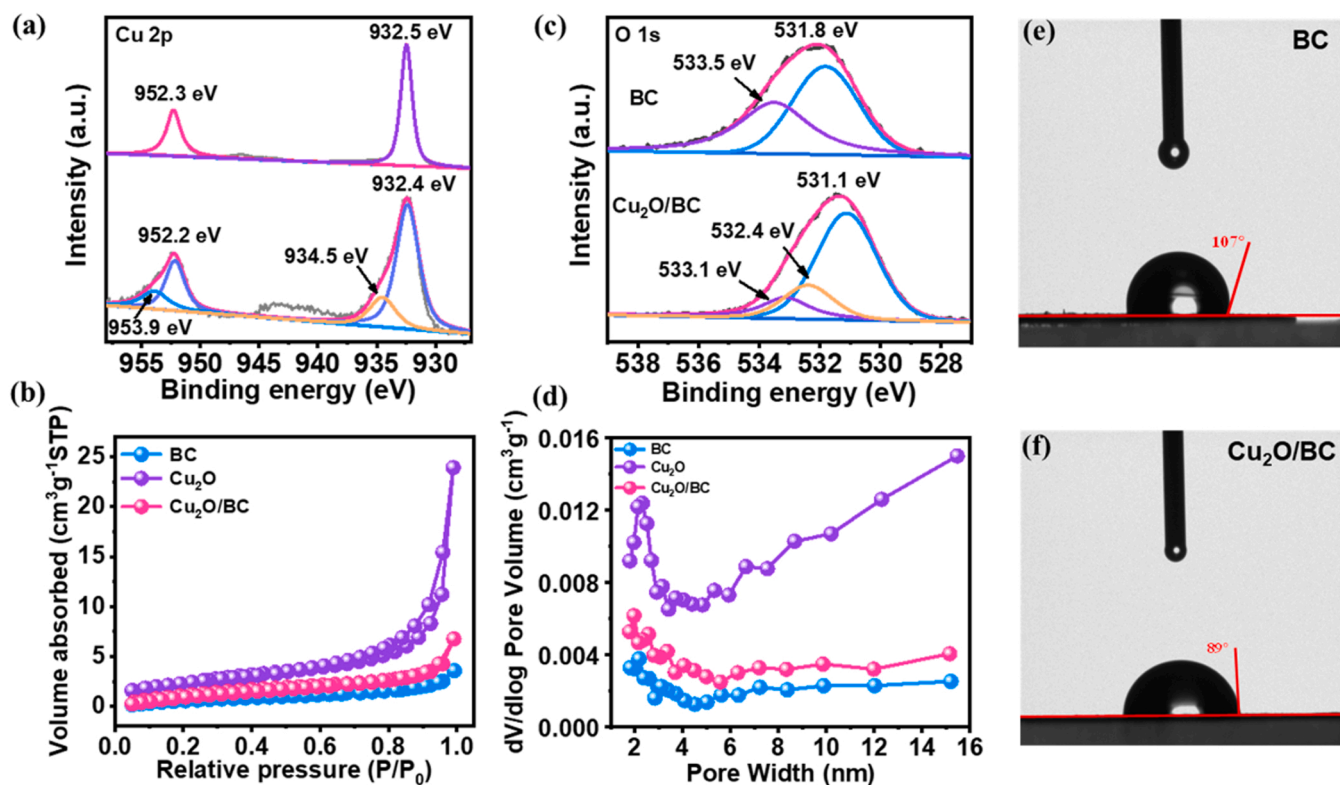
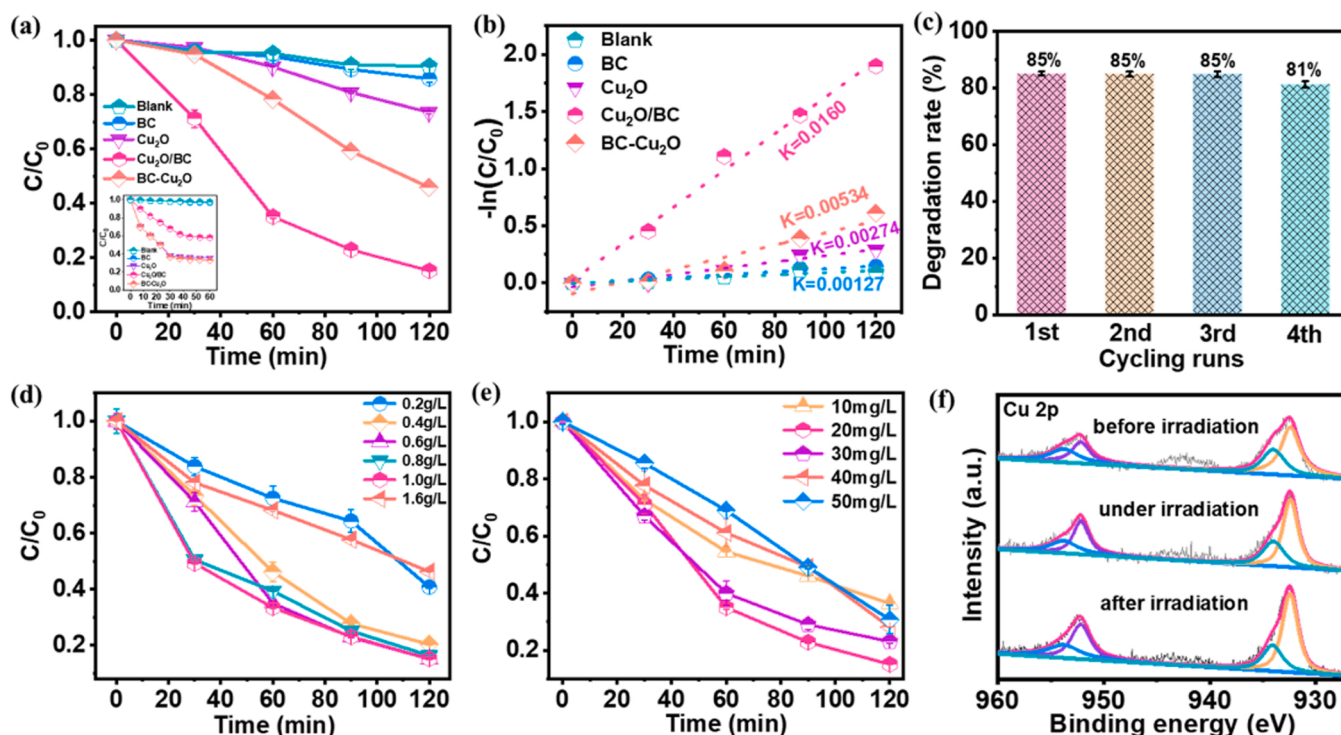


Fig. 2. a) High resolution Cu 2p spectra of  $\text{Cu}_2\text{O}$  nanoparticles and  $\text{Cu}_2\text{O}/\text{BC}$ . b) High resolution O 1s spectra of BC and  $\text{Cu}_2\text{O}/\text{BC}$ . c) Nitrogen adsorption/Desorption curve and d) the pore width distribution curves of BC,  $\text{Cu}_2\text{O}$  and  $\text{Cu}_2\text{O}/\text{BC}$ . e, f) Water contact angle of BC and  $\text{Cu}_2\text{O}/\text{BC}$ .





**Fig. 3.** a) Photocatalytic degradation curves of TC (insert picture: the adsorption performance of the catalysts). b) Pseudo-first-order kinetics for the degradation of TC by different photocatalysts under visible light irradiation. (TC: 20 mg L<sup>-1</sup>, Catalyst: 0.6 g L<sup>-1</sup>, Temperature: 20 °C, pH: 6.5, Light intensity: 250 mw/cm<sup>2</sup>). c) The cycling experiment for the degradation of TC (20 mg L<sup>-1</sup>) by Cu<sub>2</sub>O/BC. The TC removal efficiency using Cu<sub>2</sub>O/BC. d) under different catalyst dosages and e) under different concentrations of TC. f) In situ high-resolution XPS spectra of Cu 2p of Cu<sub>2</sub>O/BC.

the photocatalytic degradation of TC, the Cu<sub>2</sub>O/BC sample was reused four times under the same reaction condition (Fig. 3c). After four cycles, the Cu<sub>2</sub>O/BC sample still performed a good photocatalytic activity for the degradation of TC, and the efficiency remained at 81%. The decrease in catalytic activity after four cycles is due to the separation of some Cu<sub>2</sub>O from BC and a low amount of oxidation production from Cu<sub>2</sub>O after long-time irradiation and repeated washing. The SEM images (Fig. S8 a, b), XRD pattern (Fig. S9a), FTIR spectra (Fig. S9b) of the used photocatalyst, and in situ high-resolution XPS spectra (Fig. 3f) of Cu 2p of the Cu<sub>2</sub>O/BC manifested that the phase structure and chemical composition of Cu<sub>2</sub>O/BC did not change significantly after the photocatalytic reaction. The above results demonstrate that the Cu<sub>2</sub>O/BC composite exhibits excellent recyclability and stability, and it can be used as a potential photocatalyst with practical application value for the efficient photocatalytic degradation of pollutants.

To further investigate the photocatalytic performance of the Cu<sub>2</sub>O/BC sample, a series of condition experiments were conducted. Optimal photocatalyst dosage is useful from a practical perspective. The effect of Cu<sub>2</sub>O/BC dosage between 0.20 g L<sup>-1</sup> and 1.6 g L<sup>-1</sup> was evaluated at the TC concentration of 20 mg L<sup>-1</sup> (Fig. 3d). The removal efficiency of TC first increased and then decreased with the increase of Cu<sub>2</sub>O/BC dosage. The non-monotonic relationship between the concentration of Cu<sub>2</sub>O/BC and the degradation efficiency was attributed to the fact that more photocatalysts provide more active sites for the generation of strong oxidation free radicals, while the further introduction of catalysts increases the turbidity of the solution, reducing the transmittance of the solution and inhibiting its degradation efficiency [33]. Herein, considering the cost of practical application, the photocatalyst dosage of 0.60 g L<sup>-1</sup> was picked out as the optimal dosage for the subsequent investigations. Moreover, the concentration of TC in the natural environment varies greatly, so it is extremely essential to investigate the effect of initial TC concentration on photocatalytic performance. When the initial concentration of TC was increased from 20 mg L<sup>-1</sup> to 50 mg L<sup>-1</sup>, the removal rate of TC decreased from 85% to 69% (Fig. 3e),

respectively. This is due to the decrease in transmittance at higher initial concentrations resulting in fewer photons that can be transferred to the catalyst surface [35]. Meanwhile, competition between TC molecules and intermediates was intensified with the increasing TC concentration, competing for the limited adsorption and catalytic sites on the catalyst surface, leading to the inhibition of degradation efficiency [36]. Therefore, the initial concentration of TC of 20 mg L<sup>-1</sup> was selected for the study.

### 3.3. Real environment simulation for practical applications

To further explore the application potential of Cu<sub>2</sub>O/BC in the real environment, the following simulated real-environment experiments were carried out. As we all know, the pH value of solution varies greatly in different water bodies, and the temperature changes significantly in different seasons. It is necessary to evaluate the effect of pH and temperature on TC degradation (Fig. 4a, b). The Cu<sub>2</sub>O/BC maintains relatively good removal efficiency towards TC in wide ranges of temperature and pH value, which verifies the universal applicability of the Cu<sub>2</sub>O/BC. In addition, since surface water and actual wastewater generally contain various inorganic anions (Cl<sup>-</sup>, SO<sub>4</sub><sup>2-</sup>, HCO<sub>3</sub><sup>-</sup>, CO<sub>3</sub><sup>2-</sup>, PO<sub>4</sub><sup>3-</sup>), it is imperative to systematically evaluate the effect of their presence on TC degradation. Different ions (Cl<sup>-</sup>, SO<sub>4</sub><sup>2-</sup>, HCO<sub>3</sub><sup>-</sup>, CO<sub>3</sub><sup>2-</sup>, PO<sub>4</sub><sup>3-</sup>) were added into the TC solution at a concentration of 1 mg L<sup>-1</sup>. Fig. 4c shows that Cl<sup>-</sup> had little effect on photocatalytic removal efficiency, SO<sub>4</sub><sup>2-</sup> and HCO<sub>3</sub><sup>-</sup> had a slight inhibitory effect, while CO<sub>3</sub><sup>2-</sup> and PO<sub>4</sub><sup>3-</sup> had an obvious inhibitory effect. These results confirm that different ionic species have varying degrees of influence, but none of them have great inhibition on the photocatalytic degradation process, further demonstrating the extensive adaptability of Cu<sub>2</sub>O/BC. Furthermore, tetracycline typically coexists with naturally dissolved organics in natural water. Humic acid (HA) is normally employed to explore the influence of the coexisting organic substances [37]. Compared with the condition without HA, the removal efficiency of TC was reduced at concentrations of HA between 0.2 mg L<sup>-1</sup> and

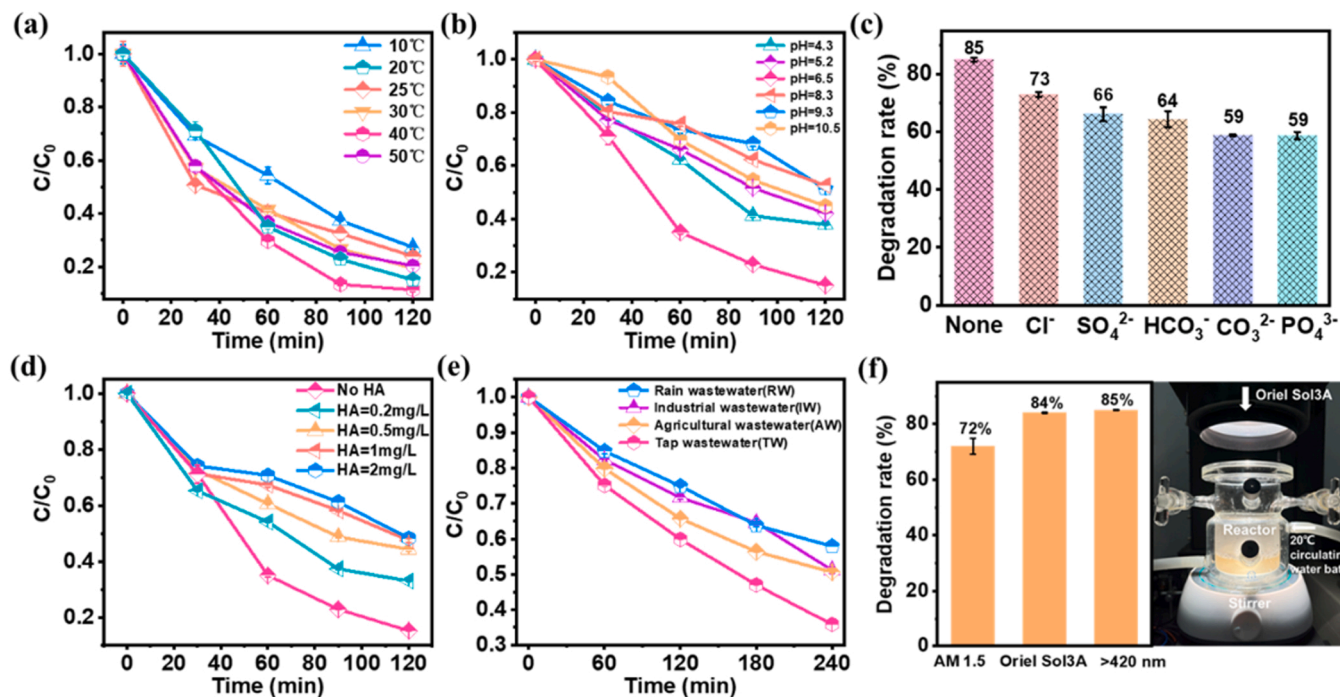


**Fig. 4.** a) Tetracycline removal efficiency using  $\text{Cu}_2\text{O}/\text{BC}$  under different temperatures and b) under different pH and c) under different inorganic anions and d) under different concentrations of HA and e) under different water matrices (RW: Rain wastewater; IW: Industrial wastewater; AW: Agricultural wastewater; TW: Tap wastewater) and f) under different light irradiation. (TC:  $20 \text{ mg L}^{-1}$ , Catalyst:  $0.6 \text{ g L}^{-1}$ , Light intensity:  $250 \text{ mw/cm}^2$ ).

$2 \text{ mg L}^{-1}$  (Fig. 4d), which may be due to the competition reaction with ROS between self-degradation of humic acid and TC [38]. To evaluate the practical feasibility of photocatalytic degradation of TC by  $\text{Cu}_2\text{O}/\text{BC}$ , various natural water and practical wastewater were investigated. Fig. 4e reveals the effect of four water substrates on TC degradation in 240 min, the degradation efficiency was the highest for TW (64%), followed by AW (49%), IW (49%), and RW (42%), manifesting that  $\text{Cu}_2\text{O}/\text{BC}$  has great potential in practical wastewater treatment. To better simulate the impact of light irradiation on TC degradation efficiency, comparative experiments were conducted with different filters and light sources. Fig. 4f displays the degradation efficiency of  $\text{Cu}_2\text{O}/\text{BC}$  for TC under different light conditions. When  $\text{Cu}_2\text{O}/\text{BC}$  was irradiated under visible light ( $\lambda > 420 \text{ nm}$ ) for 120 min, the degradation rate of TC was 85%. The degradation efficiency of TC reached 72% and 84% under the condition of AM 1.5 filter and simulated solar light source (Oriel Sol3A), respectively, suggesting that  $\text{Cu}_2\text{O}/\text{BC}$  can efficiently absorb sunlight and has enormous potential in practical application.

### 3.4. Optical properties

The study of optical properties has proven to be an important factor in the effective assessment of the photocatalytic activity of catalysts [39]. This helps to determine the absorption rate of photons and thus to better understand the photocatalytic ability of the catalyst. The total absorption of radiant energy depends on the geometry of the reactor [40] and the optical properties of the catalyst [41]. In this study, the six-flux model (described in) [42,43] are used to determine the adsorption capacity of each catalyst for radiant energy. The investigation of optical parameters such as optical thickness ( $\tau_{\text{app}}$ ), local volume photon absorption rate (LVRPA) and total photon absorption rate (TRPA) is a comprehensive approach to analyze the degradation efficiency.

### 3.5. Local volumetric rate of photon absorption

According to the reported literature, the local volumetric rate of

photon absorption (LVRPA) provides a better measure of photon absorption in the local coordinate system of the reactor [41,42]. Prior to determining the LVRPA, the optical thickness of the synthesized catalyst is calculated (Eqs. 3–7).

$$\kappa^* = \frac{\int_{\lambda_{\min}}^{\lambda_{\max}} \kappa_{\lambda}^* I_{\lambda} d\lambda}{\int_{\lambda_{\min}}^{\lambda_{\max}} I_{\lambda} d\lambda} \quad (3)$$

$$\sigma^* = \frac{\int_{\lambda_{\min}}^{\lambda_{\max}} \sigma_{\lambda}^* I_{\lambda} d\lambda}{\int_{\lambda_{\min}}^{\lambda_{\max}} I_{\lambda} d\lambda} \quad (4)$$

$$\tau = (\sigma^* + \kappa^*) C_{\text{cat}} L \quad (5)$$

$$\beta^* = \sigma^* + \kappa^* \quad (6)$$

Where  $\sigma^*$  and  $\kappa^*$  are the spectral averaged specific scattering and absorption coefficients,  $C_{\text{cat}}$  is the photocatalyst loading and  $L$  is the characteristic length for the extinction of the light inside the reactor. The scattering ( $\sigma^*$ ), absorption ( $\kappa^*$ ) and extinction ( $\beta^*$ ) coefficients obtained are shown in Table 1.

The apparent optical thickness  $\tau_{\text{app}}$  is:

$$\tau_{\text{app}} = a\tau \sqrt{1 - \omega_{\text{corr}}^2} \quad (7)$$

Eq. (8–12) are used to quantify the local volumetric rate of photon absorption (LVRPA). As shown in Table 2, the optical thickness of all catalysts is approximately linear and positively correlated with the concentration. The LVRPA on the catalyst surface also increases linearly with increasing concentration (Fig. 5a), with  $\text{Cu}_2\text{O}/\text{BC}$  having the

**Table 1**  
Optical properties of the catalyst.

Photocatalyst	$\kappa^*$ ( $\text{m}^2/\text{kg}$ )	$\sigma^*$ ( $\text{m}^2/\text{kg}$ )	$\beta^*$ ( $\text{m}^2/\text{kg}$ )
BC	632	739	1371
$\text{Cu}_2\text{O}$	321	926	1247
$\text{Cu}_2\text{O}/\text{BC}$	624	1023	1647

**Table 2**

Catalyst concentration dependent optical thickness.

Concentration (g L <sup>-1</sup> )	BC	Cu <sub>2</sub> O	Cu <sub>2</sub> O/BC
0.2	1.2846	0.9562	1.3935
0.4	2.5692	1.9124	2.7870
0.6	3.8538	2.8686	4.1805
0.8	5.1384	3.8248	5.5740
1	6.4230	4.7810	6.9675
1.6	10.277	7.6496	11.148

highest slope, followed by BC and Cu<sub>2</sub>O.

$$\text{LVRPA} = \frac{I_0 \tau_{\text{app}}}{\omega_{\text{corr}} (1 - \gamma) L} \left[ (\omega_{\text{corr}} - 1 + \sqrt{1 - \omega_{\text{corr}}^2}) e^{-\frac{\gamma \tau_{\text{app}}}{L}} + \gamma (\omega_{\text{corr}} - 1 - \sqrt{1 - \omega_{\text{corr}}^2}) e^{\frac{\gamma \tau_{\text{app}}}{L}} \right] \quad (8)$$

Where a, b,  $\omega_{\text{corr}}$  and  $\gamma$  are SFM parameters defined as follows:

$$a = 1 - \omega p_f - \frac{4\omega^2 p_s^2}{1 - \omega p_f - \omega p_b - 2\omega p_s} \quad (9)$$

$$b = \omega p_b + \frac{4\omega^2 p_s^2}{1 - \omega p_f - \omega p_b - 2\omega p_s} \quad (10)$$

$$\omega_{\text{corr}} = \frac{b}{a} \quad (11)$$

$$\gamma = \frac{1 - \sqrt{1 - \omega_{\text{corr}}^2}}{1 + \sqrt{1 - \omega_{\text{corr}}^2}} e^{-2\tau_{\text{app}}} \quad (12)$$

$$\text{TRPA} = \int_0^L \text{LVRPA} \cdot dx \quad (13)$$

The scattering probabilities  $p_f$ ,  $p_b$  and  $p_s$  are determined from the Henyey-Greenstein phase function for each photocatalyst, according to the procedure described elsewhere [44].

### 3.6. Total rate of photon absorption

Total rate of photon absorption (TRPA) is the total radiation absorbed over the entire reactor volume and is a useful parameter for determining the efficiency of the photoreactor and the optimal photocatalyst concentration for operating the photoreactor. TRPA is calculated by integrating LVRPA over the reactor length (Eq. 13). As shown in Fig. 5b, the TRPA values increase in a gradient with increasing catalyst concentration, but all only reach a constant absorption rate. It has been reported in the literature that the region where the absorption reaches a constant value (TRPA variation <0.5%) is considered to be the optimum

value [41]. For both Cu<sub>2</sub>O/BC and BC catalysts, the optimum value are around 0.6–0.8 g L<sup>-1</sup>. And for Cu<sub>2</sub>O, the optimum value is around 0.8–1 g L<sup>-1</sup>, which matches with the table of  $\tau_{\text{app}}$  (Table 2), and these values are in the range of the optimum optical thickness values (1.8–4.4) for the reactor [39,41]. Obviously, it is inaccurate to compare the activity of photocatalytic materials using the same catalyst concentration in suspension, because different materials have different optical properties and photon absorption rates. Therefore, to better compare the performance of BC, Cu<sub>2</sub>O and Cu<sub>2</sub>O/BC catalysts, we conduct comparison experiments at the optimum value of optical thickness of each catalyst. The results are in general agreement with Fig. 3a, which is not surprising, as the Cu<sub>2</sub>O monomer is easily agglomerated and unstable, and increasing the dosage can hardly improve the degradation performance.

### 3.7. photoelectrochemical properties

To elucidate the reasons for the enhanced photocatalytic performance of Cu<sub>2</sub>O/BC, optical and photoelectrochemical characterizations were performed. The UV-vis DRS of BC, Cu<sub>2</sub>O, and Cu<sub>2</sub>O/BC are presented in Fig. 6a. The light absorption property of Cu<sub>2</sub>O/BC in the wavelength range of 200 ~ 800 nm is enhanced compared to Cu<sub>2</sub>O, indicating that Cu<sub>2</sub>O/BC could efficiently utilize visible light. Compared with the transient photocurrent response of BC and BC-Cu<sub>2</sub>O (Fig. 6b), Cu<sub>2</sub>O/BC exhibited high and stable photocurrent intensity, further verifying the existence of electronic conduction between BC and Cu<sub>2</sub>O and the separation of photogenerated electron-hole pairs becomes easier [45]. According to previous reports that the smaller the radius of the semicircle, the higher the inhibition efficiency of charge recombination [46,47]. The Cu<sub>2</sub>O/BC shows the smallest radius (Fig. 6c), which has prominent charge transfer kinetics [48,49]. Photoluminescence (PL) intensity is a powerful tool for detecting photoexcited electron transfer, the Cu<sub>2</sub>O/BC exhibits much weaker PL emission than BC (Fig. 6d), demonstrating that Cu<sub>2</sub>O/BC could effectively inhibit charge carrier recombination [50–52].

### 3.8. Reactive radicals involved in the photocatalytic process

To shed light on the contribution of reactive species generated by the Cu<sub>2</sub>O/BC in the process of photocatalytic degradation, trapping experiments were performed to deeply explore the degradation mechanism. Triethanolamine (TEOA), silver nitrate (AgNO<sub>3</sub>), isopropanol (IPA), L-tryptophan, and 4-hydroxy-2, 2, 6, 6-tetramethylpiperidine-N-oxyl (TEMPO) (Fig. 7a) were served as the scavengers for holes (h<sup>+</sup>), electrons (e<sup>-</sup>), hydroxyl radicals (·OH), singlet oxygen (<sup>1</sup>O<sub>2</sub>) and superoxide radicals (·O<sub>2</sub><sup>-</sup>), respectively. Compared with TC degradation efficiency without using any scavenger (85%) (Fig. 7b), the addition of L-

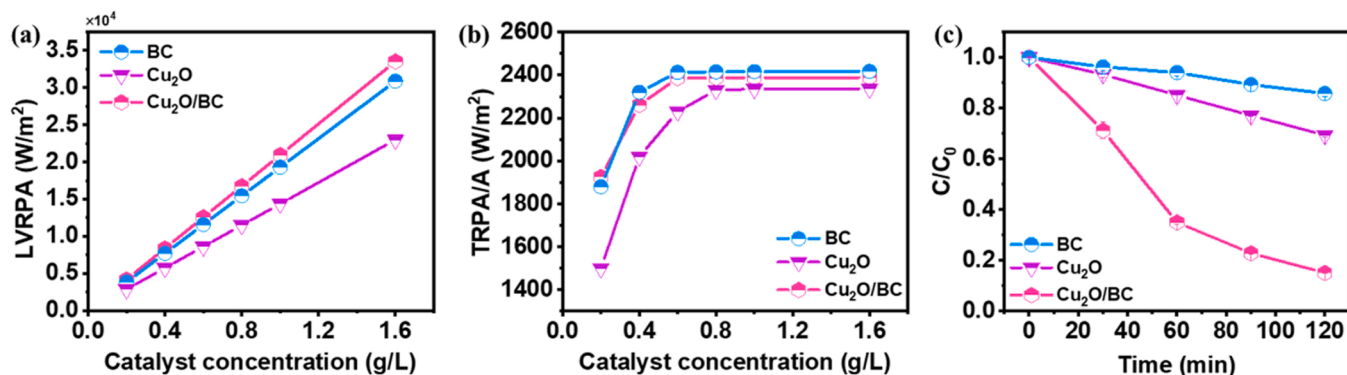


**Fig. 5.** a) LVRPA at the surface with different catalyst concentration. b) Catalyst concentration dependent TRPA/A profile. c) Photocatalytic degradation of TC in the suspension catalytic system with the optimum value of optical thickness of each catalyst (BC, Cu<sub>2</sub>O and Cu<sub>2</sub>O/BC catalyst dosages are 0.6, 0.8, and 0.6 g L<sup>-1</sup>, respectively).



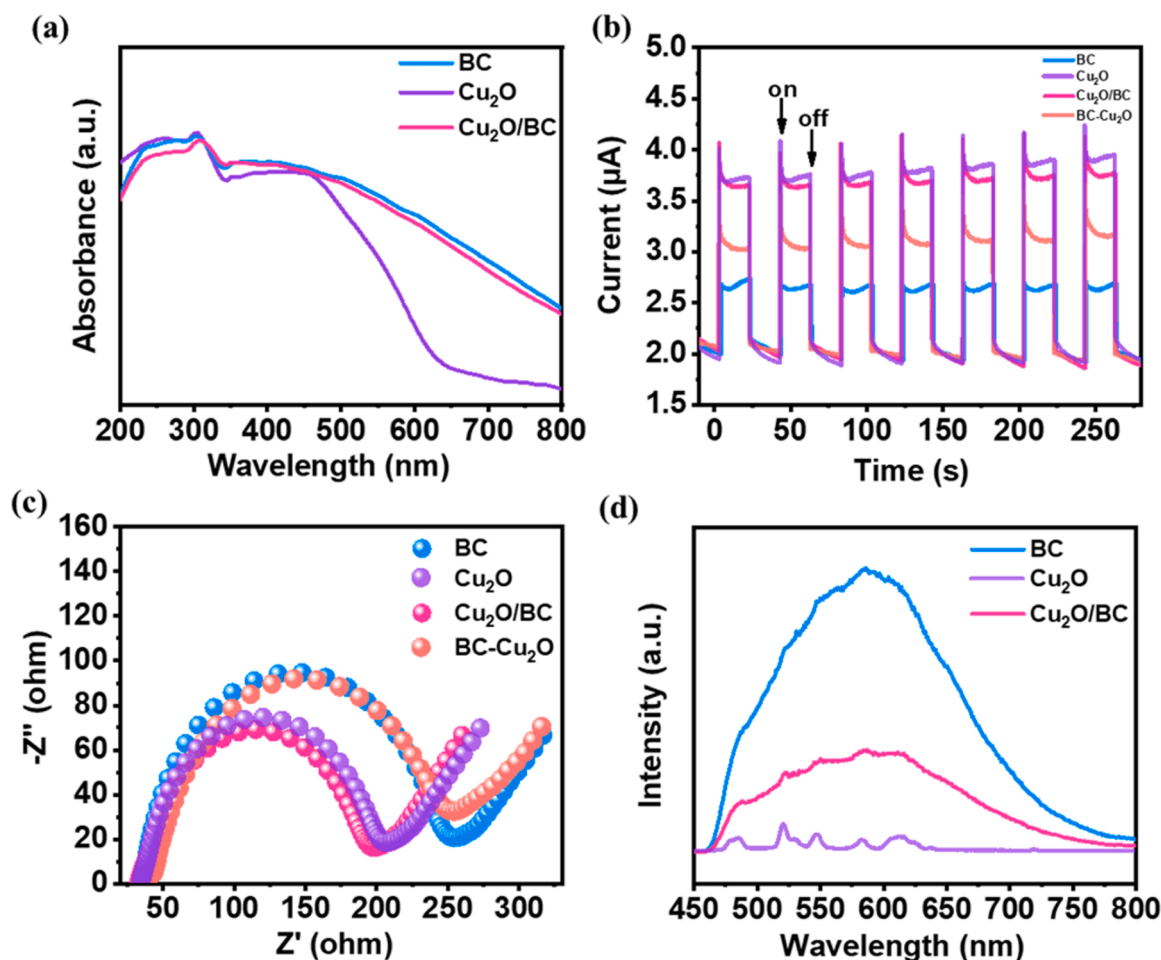


Fig. 6. a) UV-vis DRS spectra. b) photocurrent responses spectra. c) EIS Nyquist plots and d) PL spectra of the samples.

tryptophan almost completely suppressed the degradation efficiency of TC (only 4.4% of TC was removed within 120 min). When TEOA, TEMPO, AgNO<sub>3</sub>, and IPA were presented in the photocatalytic system, the corresponding removal efficiencies were reduced to 40.0%, 44.4%, 52.5%, and 62.3%, respectively. These results suggest that <sup>1</sup>O<sub>2</sub> plays a dominant role in the degradation process, and other active species play a secondary role. In addition, the generation of active species on Cu<sub>2</sub>O/BC was monitored more intuitively using 5,5-dimethyl-1-pyrroline N-oxide (DMPO), the 2,2,6,6-tetramethylpiperidine-1-oxyl (TEMPO), and 2,2,6,6-tetramethylpiperidine (TEMP) spin-trapping ESR techniques. The 1:1:1 signal peak corresponds to the production of photogenerated holes (Fig. 7c), and the intensity of the TEMPO-h<sup>+</sup> signal diminishes after illumination, indicating that the holes are continuously consumed with the occurrence of the reaction.[47] Similarly, the 1:2:2:1, and 1:1:1 signal peaks (Fig. 7d,e) correspond to DMPO-O<sub>2</sub> and TEMP-<sup>1</sup>O<sub>2</sub>, respectively. The absence of signal in the dark reaction and the enhancement of signal after illumination suggests that the energy band structure of the Cu<sub>2</sub>O/BC is compatible with the generation of these ROS, which further confirms the results of the ROS trapping experiments.

### 3.9. Possible charge transfer mechanism in the Cu<sub>2</sub>O/BC system

The band structure characterization allowed us to further investigate the generation of ROS by Cu<sub>2</sub>O/BC. According to the UV-Vis absorption band edge (Fig. S10a, b), the band gaps of BC and Cu<sub>2</sub>O were estimated to be 1.61 eV and 1.96 eV, respectively. The valence band potential of BC and Cu<sub>2</sub>O were 0.53 V and 1.1 V (vs. NHE), respectively

(Fig. 7h, f), which were reflected by the UPS valence band spectroscopy. Based on the calculated band gap, the conduction band potential of BC and Cu<sub>2</sub>O were determined to be -1.08 V and -0.86 V (vs. NHE), respectively.

According to the above analytical results, we propose a possible charge transfer mechanism for the Cu<sub>2</sub>O/BC (Fig. 7g). The Cu<sub>2</sub>O/BC generates electrons and holes under visible light irradiation (Eq. S1), and some of these holes can be directly involved in the decomposition process of TC molecules. The CB edge potential of Cu<sub>2</sub>O (-0.86 V vs. NHE) is more negative than the standard redox potential of O<sub>2</sub>/·O<sub>2</sub> (-0.33 V vs. NHE), which means that electrons on CB can combine with molecular oxygen to form ·O<sub>2</sub> (Eq. S2). ·O<sub>2</sub> can also directly participate in the degradation process of TC. The VB edge potential of BC (0.53 V vs. NHE) is more positive than the standard redox potential of ·O<sub>2</sub>/<sup>1</sup>O<sub>2</sub> (0.34 V vs. NHE), indicating that ·O<sub>2</sub> can combine with h<sup>+</sup> to generate <sup>1</sup>O<sub>2</sub> (Eq. S3). Meanwhile, <sup>1</sup>O<sub>2</sub> can be effectively produced by the photosensitive excitation of ambient triplet-state oxygen (Eq. S4) [38]. Since the potential of OH<sup>-</sup>/·OH (2.40 V vs NHE) is more positive than both Cu<sub>2</sub>O and BC, ·OH cannot be formed under visible light irradiation, but ·OH can also be produced by the two-step reaction of ·O<sub>2</sub> (Eqs. S5, 6) [53]. Therefore, the enhanced photocatalytic performance of Cu<sub>2</sub>O/BC can be attributed to the formation of a type-II band structure between Cu<sub>2</sub>O and BC, which accelerates the separation of photogenerated electron-hole pairs during the reaction.

### 3.10. Possible degradation mechanism and pathways of TC

To investigate the pathways of the photocatalytic TC degradation

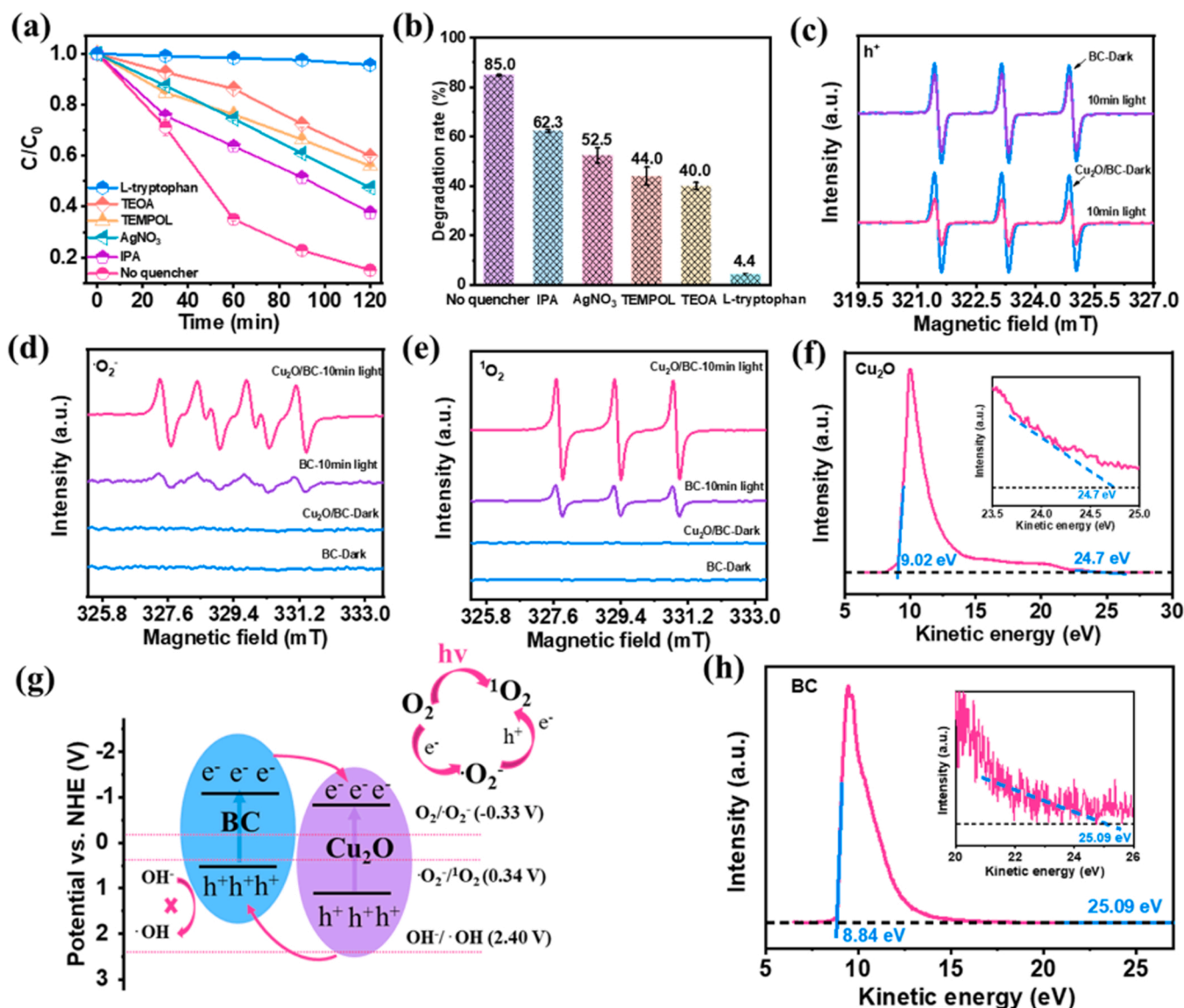


Fig. 7. a, b) Roles of different reactive species scavengers (1 mM) on the removal of TC by the Cu<sub>2</sub>O/BC under visible-light irradiation. (TC: 20 mg L<sup>-1</sup>, Catalyst: 0.6 g L<sup>-1</sup>, Temperature: 20 °C, pH: 6.5, Light intensity: 250 mw/cm<sup>2</sup>). c-e) ESR spectra of radical species ( $h^+$ ,  $\cdot O_2^-$ , and  $^1O_2$ ). f) UPS valence band (VB) spectra of Cu<sub>2</sub>O. g) Schematic diagram of the energy band structure of and possible charge transfer mechanism of Cu<sub>2</sub>O/BC. h) UPS valence band (VB) spectra of BC.

process in depth, LC-MS was carried out to identify the degradation intermediates of TC in the presence of Cu<sub>2</sub>O/BC. The mass spectra is shown in Fig. S12. Based on the detected intermediates and related reports, two possible TC degradation pathways were proposed and described in Fig. 8. Pathway I is continuous fragmentation induced by reactive species. The formation of TC 1 is attributed to the deamidation of TC, and the absence of the dimethylamino group in TC 1 forms TC 2. Then TC 2 is cleaved to TC 3 by ring-opening and dealcoholization. Finally, TC 3 is transformed into TC 4 by deacetylation [35,54]. For Pathway II, TC is converted to TC 5 by dimethylamine demethylation due to its low N-C bond energy. Subsequently, the replacement of acylamino by the carbonyl group, along with the dehydration of TC 5, producing TC 6, the carbonyl group of TC 6 is broken to produce TC 7, and the carbon ring in TC 7 is further cleaved to form TC 8. Finally, decarboxylation of TC 8 yields TC 9 [29]. The total organic carbon (TOC) measurement (Fig. S13) shows that most of the organic matter will eventually be mineralized. Therefore, the results of both of the above pathways may end up converting the respective products to CO<sub>2</sub> and H<sub>2</sub>O.

To better study the sites of reactive species attack on TC molecule

and the photocatalytic degradation pathway, the Hirshfeld charge distribution and condensed Fukui index were proposed with Gaussian and Multiwfn software. According to the Fukui function theory and our theoretical calculation results (Fig. 9), electrophilic reagents ( $h^+$ ,  $^1O_2$ ) preferentially attack 37 N (0.1076), 38 C (0.0238), and 39 C (0.0238) positions, which exhibit high  $f$  values. Thus, the transformation from TC to TC5 is subjected to attacking at 39 C-37 N-38 C, which leads to the cleavage of the C-N bond of the TC molecule with pathway II. In pathway I, the key product TC1 is generated through the nucleophilic reaction ( $\cdot O_2^-$  attacking) in the positions of 19 C (0.0105) and 27 C (0.0133), which display high  $f^-$  values. Moreover, the 37 N (0.0554), 38 C (0.0140), and 39 C (0.0139) positions also possess high  $f^0$  values, indicating that the C-N bond may likely be attacked by  $\cdot OH$ . Based on theoretical calculations and ESR results and ROS trapping experiments, the pathway II is considered to be dominant.

To further confirm the decomposition and mineralization of TC, 3D EMMs were carried out to distinguish the transformation and evolution of TC by Cu<sub>2</sub>O/BC system. As shown in Fig. 10a, no obvious fluorescence signal was observed in the initial TC solution, indicating that the TC molecule was not decomposed into other products. When the solution

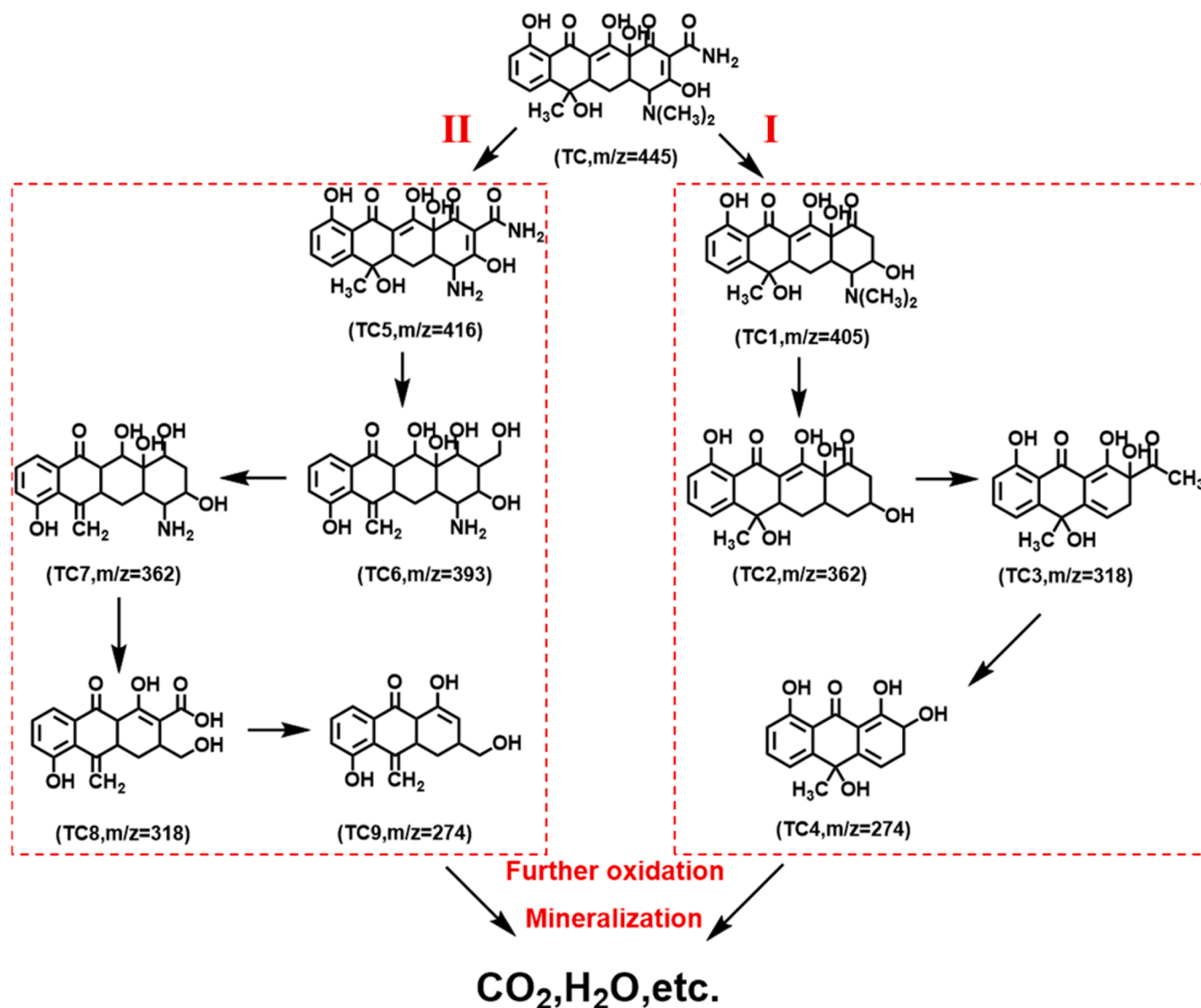


Fig. 8. Possible TC photodegradation pathway over Cu<sub>2</sub>O/BC.

was irradiated by visible light for 60 min, a fluorescence peak appeared at  $\lambda_{\text{ex}}/\lambda_{\text{em}} = (200\text{--}250\text{ nm})/(400\text{--}500\text{ nm})$  (Fig. 10b), which was attributed to the formation of fulvic acid-like compounds [55]. After 90 min illumination (Fig. 10c), the fluorescence area of fulvic acid-like became larger due to the accumulation of intermediates. Extending the illumination time to 120 min (Fig. 10d), another small new peak appeared at  $\lambda_{\text{ex}}/\lambda_{\text{em}} = (220\text{ nm})/(330\text{ nm})$ . According to the previous studies, this peak was associated with protein-like substances [56], indicating the conversion of fulvic acid-like substances to protein-like substances. After 4 h illumination (Fig. 10e), the signal of the fulvic acid-like fluorescence region almost disappeared, while the signal intensity of protein-like fluorescence region  $\lambda_{\text{ex}}/\lambda_{\text{em}} = (220\text{ nm})/(330\text{ nm})$  was further enhanced. Meanwhile, a small new peak was observed at  $\lambda_{\text{ex}}/\lambda_{\text{em}} = (280\text{ nm})/(330\text{ nm})$ , this peak also was associated with the protein-like substances [56], indicating that the degradation of fulvic acid-like almost completely. Finally, after 6 h illumination (Fig. 10f), the signal of the fulvic acid-like fluorescence region completely disappeared, and two distinct peaks of protein-like substances further strengthened, revealing that fulvic acid-like compounds were completely degraded and transformed during the photocatalysis process [57], which might eventually be evolved into CO<sub>2</sub> and H<sub>2</sub>O. These results were consistent with the proposed TC degradation

pathway.

### 3.11. Toxicity assessment

To better understand the suitability of the prepared Cu<sub>2</sub>O/BC catalyst under real environmental conditions, the toxicity effects of intermediates in the TC degradation process were investigated by their effects on the *E. coli* and *R. rubrum* bacteria. As shown in Fig. 11a, b, after 1 h photodegradation treatment, OD<sub>600</sub> values of *E. coli* and *R. rubrum* decreased slightly compared to the blank sample, indicating that TC may not be fully degraded (TC has the bacteriostatic effect). With the degradation time prolonged to 3 h, the OD<sub>600</sub> values were almost comparable to the blank one, suggesting that the toxicity of the intermediate products during TC degradation can be neglected. Moreover, the bacterial colonies number of *E. coli* and *R. rubrum* did not significantly change after the introduction of the degradation products, further demonstrating that the Cu<sub>2</sub>O/BC catalyst can degrade TC into less toxic intermediates.

## 4. Conclusion

In summary, a low-cost and facile strategy was developed to prepare



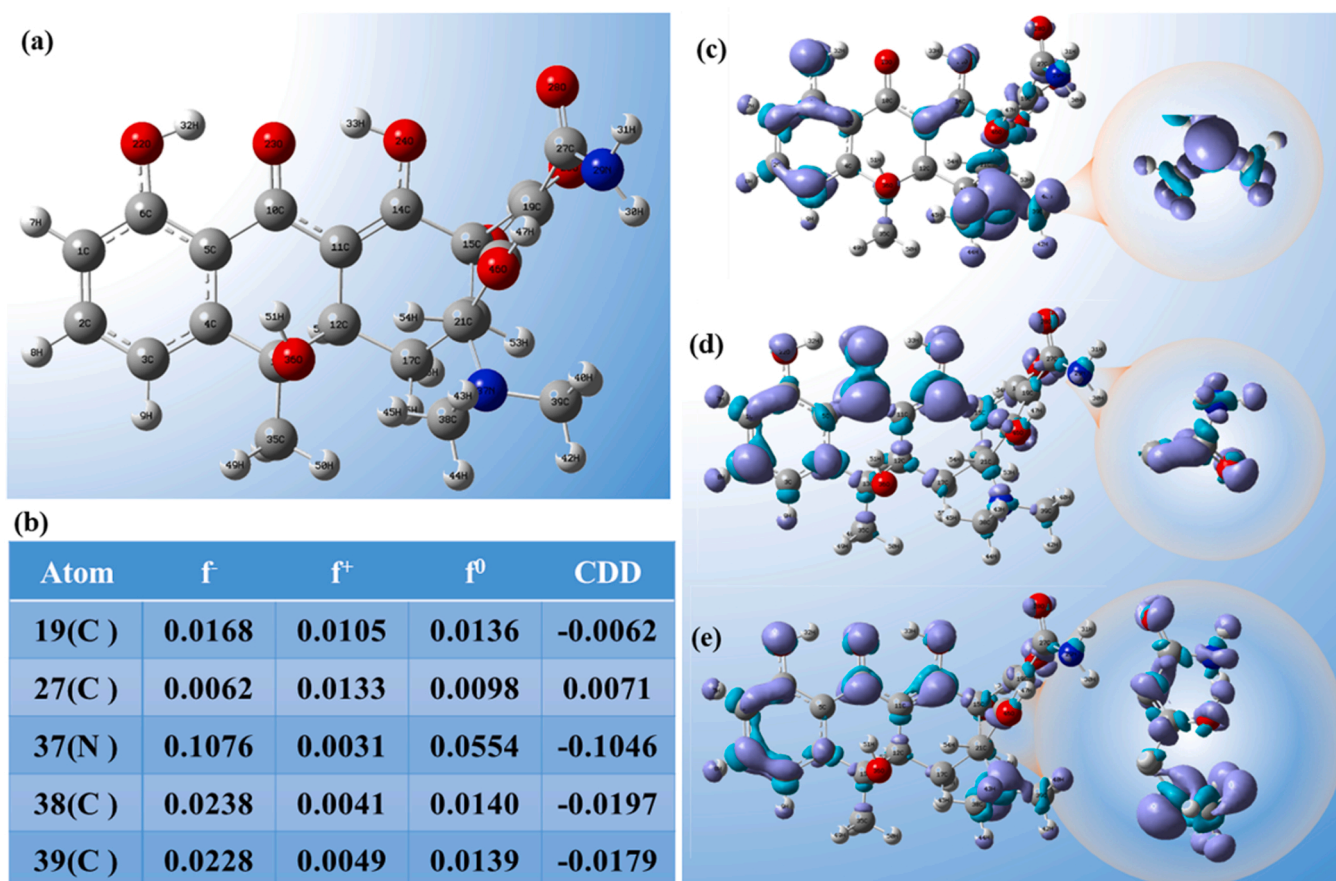


Fig. 9. a) The atomic structure configuration of TC. b) Fukui index of TC. c-e) The isosurface of Fukui index for TC. The value of the isosurface of the entire TC molecule and local molecule are 0.02 and 0.01, respectively.

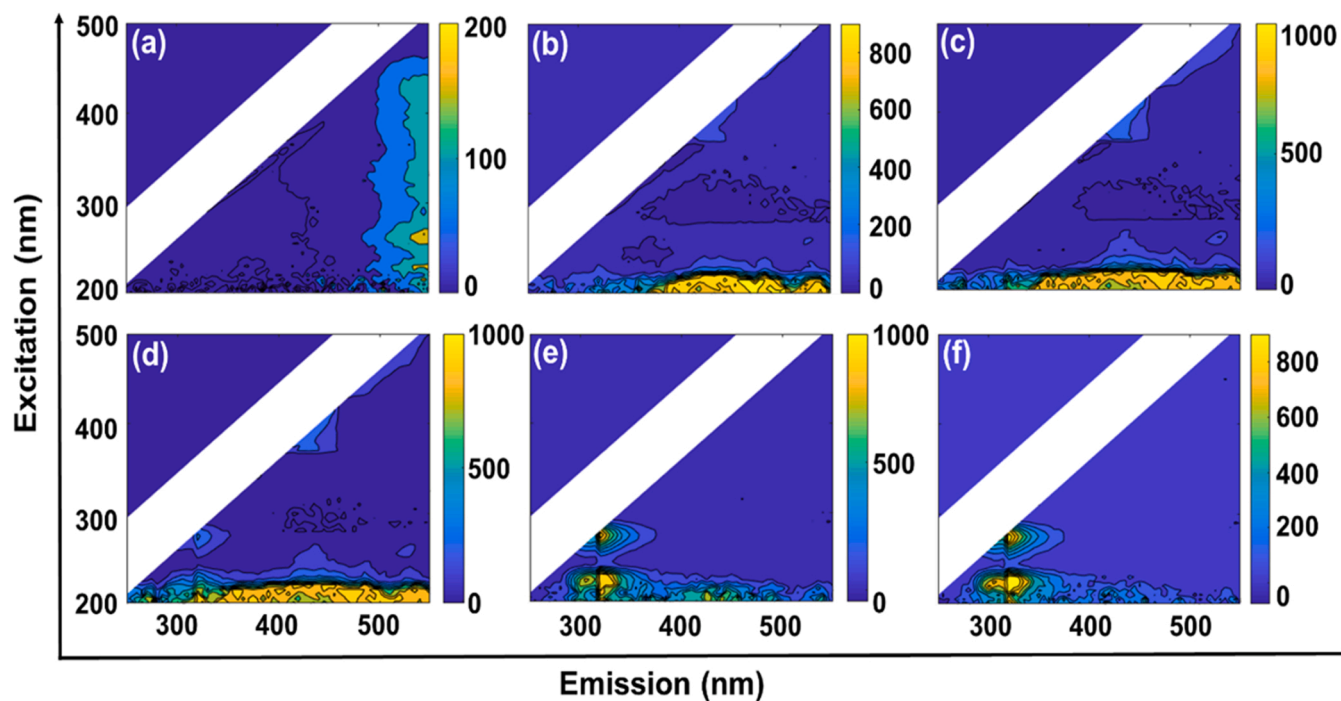
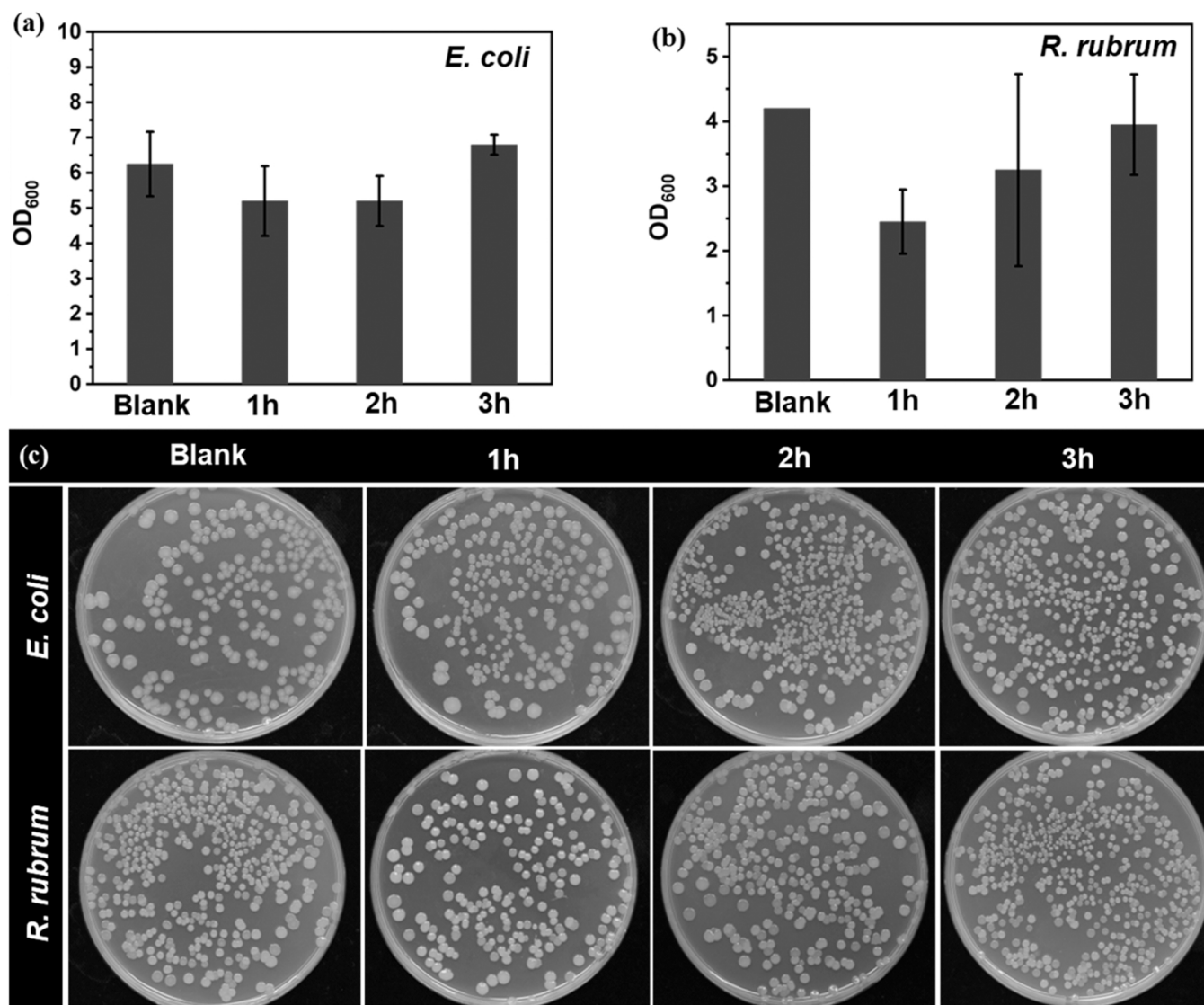


Fig. 10. Three-dimensional excitation-emission matrix fluorescence spectroscopy (3D EEMs) of the TC aqueous solution a) taken from the original solution and b–f) collected after visible light irradiation times of 60, 90, 120, 240 and 480 min, respectively.



**Fig. 11.** a, b) OD<sub>600</sub>, and c) photographs of bacterial colonies of *E. coli* and *R. rubrum* with the addition of TC solution treated in Cu<sub>2</sub>O/BC for a different time and blank (without adding TC solution).

Cu<sub>2</sub>O/BC photocatalysts for solar-driven photocatalytic degradation of TC. The Cu<sub>2</sub>O/BC exhibits excellent photocatalytic activity towards the degradation of tetracycline under visible-light irradiation, the degradation rate is roughly 6.0 and 3.2 times higher than BC and Cu<sub>2</sub>O. The enhanced performance is attributed to the construction of heterojunction, which promotes the effective separation of photogenerated carriers. In addition, the three-dimensional hollow BC with spatial domain confinement ensures the structural stability of Cu<sub>2</sub>O. The applicability of Cu<sub>2</sub>O/BC photocatalysts in a wide temperature and pH range as well as various inorganic ions and organic substance (HA) validates its application potential. Meanwhile, the Cu<sub>2</sub>O/BC catalysts also show great potential in real wastewater treatment. The mechanism study indicates that <sup>1</sup>O<sub>2</sub> is the most important contributor to the TC removal process. The LC-MS intermediate analysis and DFT calculation manifest that the pathway attacking the N methyl of TC is the dominant pathway in the degradation process. The 3DEEMs techniques and antibacterial experimental (against *E. coli* and *R. rubrum*) results demonstrate that TC is mainly degraded into less toxic fulvic acid-like and protein-like substances. This work elucidates the degradation conversion process of TC and provides new insight into the synthesis of high-performance photocatalysts by combining semiconductors with earth-rich biomaterials.

## Supporting Information

Supporting Information is available from the author.

## CRediT authorship contribution statement

**Zhiqian Zhang:** Data curation, Formal analysis, Investigation, Writing – original draft. **Jianli Liang:** Validation, Formal analysis. **Wei Zhang:** Software. **Min Zhou:** Formal analysis. **Xianglin Zhu:** Formal analysis. **Zheyang Liu:** Formal analysis. **Yang Li:** Formal analysis. **Zhiqiang Guan:** Formal analysis. **Chun-Sing Lee:** Writing – review & editing. **Po Keung Wong:** Writing – review & editing. **Huaming Li:** Supervision, Writing – review & editing. **Zhifeng Jiang:** Conceptualization, Formal analysis, Investigation, Methodology, Resources, Supervision, Funding acquisition, Writing – review & editing.

## Declaration of Competing Interest

The authors declare that they have no known competing financial interests or personal relationships that could have appeared to influence the work reported in this paper.

## Data Availability

Data will be made available on request.

## Acknowledgements

This work was supported by National Natural Science Foundation of China (Grant No. 22178149), Jiangsu Distinguished Professor Program, Natural Science Foundation of Jiangsu Province for Outstanding Youth Scientists (BK20211599), Key R&D Project of Zhenjiang City (CQ2022001), and Scientific Research Startup Foundation of Jiangsu University (No. 202096).

## Appendix A. Supporting information

Supplementary data associated with this article can be found in the online version at [doi:10.1016/j.apcatb.2023.122621](https://doi.org/10.1016/j.apcatb.2023.122621).

## References

- [1] Q. Zhang, J. Chen, X. Gao, H. Che, P. Wang, Y. Ao, In-depth insight into the mechanism on photocatalytic synergistic removal of antibiotics and Cr (VI): The decisive effect of antibiotic molecular structure, *Appl. Catal. B: Environ.* 313 (2022), 121443.
- [2] Q. Wu, H. Yang, L. Kang, Z. Gao, F. Ren, Fe-based metal-organic frameworks as Fenton-like catalysts for highly efficient degradation of tetracycline hydrochloride over a wide pH range: acceleration of Fe(II)/Fe(III) cycle under visible light irradiation, *Appl. Catal. B: Environ.* 263 (2020), 118282.
- [3] Q. Zhang, L. Jiang, J. Wang, Y. Zhu, Y. Pu, W. Dai, Photocatalytic degradation of tetracycline antibiotics using three-dimensional network structure perylene diimide supramolecular organic photocatalyst under visible-light irradiation, *Appl. Catal. B: Environ.* 277 (2020), 119122.
- [4] Z. Xie, Y. Feng, F. Wang, D. Chen, Q. Zhang, Y. Zeng, W. Lv, G. Liu, Construction of carbon dots modified MoO<sub>3</sub>/g-C<sub>3</sub>N<sub>4</sub> Z-scheme photocatalyst with enhanced visible-light photocatalytic activity for the degradation of tetracycline, *Appl. Catal. B: Environ.* 229 (2018) 96–104.
- [5] D. Gogoi, R.S. Karmur, M.R. Das, N.N. Ghosh, Cu and CoFe<sub>2</sub>O<sub>4</sub> nanoparticles decorated hierarchical porous carbon: an excellent catalyst for reduction of nitroaromatics and microwave-assisted antibiotic degradation, *Appl. Catal. B: Environ.* 312 (2022), 121407.
- [6] C. Peiris, S.R. Gunatilake, T.E. Mlsna, D. Mohan, M. Vithanage, Biochar based removal of antibiotic sulfonamides and tetracyclines in aquatic environments: a critical review, *Bioresour. Technol.* 246 (2017) 150–159.
- [7] Z. Zhao, G. Zhang, Y. Zhang, M. Dou, Y. Li, Fe<sub>3</sub>O<sub>4</sub> accelerates tetracycline degradation during anaerobic digestion: synergistic role of adsorption and microbial metabolism, *Water Res.* 185 (2020), 116225.
- [8] Y. Zhang, H. Wang, Y. Li, B. Wang, J. Huang, S. Deng, G. Yu, Y. Wang, Removal of micropollutants by an electrochemically driven UV/chlorine process for decentralized water treatment, *Water Res.* 183 (2020), 116115.
- [9] Y. Liu, Y. Cai, G. Li, W. Wang, P.K. Wong, T. An, Response mechanisms of different antibiotic-resistant bacteria with different resistance action targets to the stress from photocatalytic oxidation, *Water Res.* 218 (2022), 118407.
- [10] Z. Yang, F. Wang, H. Guo, L.E. Peng, X.H. Ma, X.X. Song, Z. Wang, C.Y. Tang, Mechanistic insights into the role of polydopamine interlayer toward improved separation performance of polyamide nanofiltration membranes, *Environ. Sci. Technol.* 54 (2020) 11611–11621.
- [11] W. Liu, X. Li, X. Chu, S. Zuo, B. Gao, C. Yao, Z. Li, Y. Chen, Boosting photocatalytic reduction of nitrate to ammonia enabled by perovskite/biochar nanocomposites with oxygen defects and O-containing functional groups, *Chemosphere* 294 (2022), 133763.
- [12] L. Yang, S.K. Ravi, D.K. Nandakumar, F.I. Alzakia, W. Lu, Y. Zhang, J. Yang, Q. Zhang, X. Zhang, S.C. Tan, A hybrid artificial photocatalysis system splits atmospheric water for simultaneous dehumidification and power generation, *Adv. Mater.* 31 (2019), e1902963.
- [13] S. Zhang, Y. Zhao, R. Shi, C. Zhou, G.I.N. Waterhouse, Z. Wang, Y. Weng, T. Zhang, Sub-3 nm ultrafine Cu<sub>2</sub>O for visible light driven nitrogen fixation, *Angew. Chem. Int. Ed.* 60 (2021) 2554–2560.
- [14] L. Yu, G. Li, X. Zhang, X. Ba, G. Shi, Y. Li, P.K. Wong, J.C. Yu, Y. Yu, Enhanced activity and stability of carbon-decorated cuprous oxide mesoporous nanorods for CO<sub>2</sub> reduction in artificial photosynthesis, *ACS Catal.* 6 (2016) 6444–6454.
- [15] Y. Zhang, H. Lv, Z. Zhang, L. Wang, X. Wu, H. Xu, Stable unbiased photo-electrochemical overall water splitting exceeding 3% efficiency via covalent triazine framework/metal oxide hybrid photoelectrodes, *Adv. Mater.* 33 (2021), e2008264.
- [16] X. Zhao, Y. Fan, W. Zhang, X. Zhang, D. Han, L. Niu, A. Ivaska, Nanoengineering construction of Cu<sub>2</sub>O nanowire arrays encapsulated with g-C<sub>3</sub>N<sub>4</sub> as 3D spatial reticulation all-solid-state direct Z-scheme photocatalysts for photocatalytic reduction of carbon dioxide, *ACS Catal.* 10 (2020) 6367–6376.
- [17] M. Zhang, J. Wang, H. Xue, J. Zhang, S. Peng, X. Han, Y. Deng, W. Hu, Acceptor-doping accelerated charge separation in Cu<sub>2</sub>O photocathode for photoelectrochemical water splitting: theoretical and experimental studies, *Angew. Chem. Int. Ed.* 59 (2020) 18463–18467.
- [18] C. Liu, M. Zhang, J. Li, W. Xue, T. Zheng, C. Xia, J. Zeng, Nanoconfinement engineering over hollow multi-shell structured copper towards efficient electrocatalytic C-C coupling, *Angew. Chem. Int. Ed.* 61 (2022), e202113498.
- [19] Y.A. Wu, I. McNulty, C. Liu, K.C. Lau, Q. Liu, A.P. Paulikas, C.-J. Sun, Z. Cai, J. R. Guest, Y. Ren, V. Stamenkovic, L.A. Curtiss, Y. Liu, T. Rajh, Facet-dependent active sites of a single Cu<sub>2</sub>O particle photocatalyst for CO<sub>2</sub> reduction to methanol, *Nat. Energy* 4 (2019) 957–968.
- [20] T. Wei, Y.-N. Zhu, X. An, L.-M. Liu, X. Cao, H. Liu, J. Qu, Defect modulation of Z-scheme TiO<sub>2</sub>/Cu<sub>2</sub>O photocatalysts for durable water splitting, *ACS Catal.* 9 (2019) 8346–8354.
- [21] Z.F. Jiang, H.L. Sun, T.Q. Wang, B. Wang, W. Wei, H.M. Li, S.Q. Yuan, T.C. An, H. J. Zhao, J.G. Yu, P.K. Wong, Nature-based catalyst for visible-light-driven photocatalytic CO<sub>2</sub> reduction, *Energy Environ. Sci.* 11 (2018) 2382–2389.
- [22] B. Wang, Z. Jiang, J.C. Yu, Treated rape pollen: a metal-free visible-light-driven photocatalyst from nature for efficient water disinfection, *J. Mater. Chem. A* 7 (2019) 9335–9344.
- [23] K. Xiao, T. Wang, M. Sun, A. Hanif, Q. Gu, B. Tian, Z. Jiang, B. Wang, H. Sun, J. Shang, P.K. Wong, Photocatalytic bacterial inactivation by a rape pollen-MoS<sub>2</sub> biohybrid catalyst: synergetic effects and inactivation mechanisms, *Environ. Sci. Technol.* 54 (2020) 537–549.
- [24] L. Xu, Y. Liu, L. Li, Z. Hu, J.C. Yu, Fabrication of a photocatalyst with biomass waste for H<sub>2</sub>O<sub>2</sub> synthesis, *ACS Catal.* 11 (2021) 14480–14488.
- [25] X. He, N. Zheng, R. Hu, Z. Hu, J.C. Yu, Hydrothermal and pyrolytic conversion of biomasses into catalysts for advanced oxidation treatments, *Adv. Funct. Mater.* 31 (2020), 2006505.
- [26] Z. Hu, J.C. Yu, T. Ming, J. Wang, A wide-spectrum-responsive TiO<sub>2</sub> photoanode for photoelectrochemical cells, *Appl. Catal. B: Environ.* 168 169 (2015) 483–489.
- [27] D. Xia, Q. Chen, Y. Jiao, Q. Lian, M. Sun, C. He, J. Shang, T. Wang, A modified flower pollen-based photothermocatalytic process for enhanced solar water disinfection: photoelectric effect and bactericidal mechanisms, *Water Res.* 217 (2022), 118423.
- [28] Z. Tang, R. Yin, W. Qu, H. Liu, H. Luo, D. Xia, Y. Huang, L. Shu, C. He, Flower pollen-based photosensitization process for enhanced solar disinfection of drinking water: reactor design and inactivation mechanisms, *ACS EST Eng.* 2 (2022) 629–641.
- [29] Y. Wu, X. Li, H. Zhao, F. Yao, J. Cao, Z. Chen, D. Wang, Q. Yang, Core-shell structured Cu<sub>2</sub>O@HKUST-1 heterojunction photocatalyst with robust stability for highly efficient tetracycline hydrochloride degradation under visible light, *Chem. Eng. J.* 426 (2021), 131255.
- [30] H. Luo, B. Li, J.G. Ma, P. Cheng, Surface modification of nano-Cu<sub>2</sub>O for controlling CO<sub>2</sub> electrochemical reduction to ethylene and syngas, *Angew. Chem. Int. Ed.* 61 (2022), e202116736.
- [31] Y. Deng, C. Wan, C. Li, Y. Wang, X. Mu, W. Liu, Y. Huang, P.K. Wong, L. Ye, Synergy effect between facet and zero-valent copper for selectivity photocatalytic methane formation from CO<sub>2</sub>, *ACS Catal.* 12 (2022) 4526–4533.
- [32] Y. Yue, P. Zhang, W. Wang, Y. Cai, F. Tan, X. Wang, X. Qiao, P.K. Wong, Enhanced dark adsorption and visible-light-driven photocatalytic properties of narrower-band-gap Cu<sub>2</sub>S decorated Cu<sub>2</sub>O nanocomposites for efficient removal of organic pollutants, *J. Hazard. Mater.* 384 (2020), 121302.
- [33] S. Xin, S. Huo, C. Zhang, X. Ma, W. Liu, Y. Xin, M. Gao, Coupling nitrogen/oxygen self-doped biomass porous carbon cathode catalyst with CuFeO<sub>2</sub>/biochar particle catalyst for the heterogeneous visible-light driven photo-electro-Fenton degradation of tetracycline, *Appl. Catal. B: Environ.* 305 (2022), 121024.
- [34] R. Xu, M. Li, Q. Zhang, Collaborative optimization for the performance of ZnO/biochar composites on persulfate activation through plant enrichment-pyrolysis method, *Chem. Eng. J.* 429 (2022), 132294.
- [35] Y. Yang, Z. Zeng, C. Zhang, D. Huang, G. Zeng, R. Xiao, C. Lai, C. Zhou, H. Guo, W. Xue, M. Cheng, W. Wang, J. Wang, Construction of iodine vacancy-rich BiOI/Ag@AgI Z-scheme heterojunction photocatalysts for visible-light-driven tetracycline degradation: transformation pathways and mechanism insight, *Chem. Eng. J.* 349 (2018) 808–821.
- [36] F. Chen, Q. Yang, X. Li, G. Zeng, D. Wang, C. Niu, J. Zhao, H. An, T. Xie, Y. Deng, Hierarchical assembly of graphene-bridged Ag<sub>3</sub>PO<sub>4</sub>/Ag/BiVO<sub>4</sub> (040) Z-scheme photocatalyst: an efficient, sustainable and heterogeneous catalyst with enhanced visible-light photoactivity towards tetracycline degradation under visible light irradiation, *Appl. Catal. B: Environ.* 200 (2017) 330–342.
- [37] H. Wang, Y. Wu, M. Feng, W. Tu, T. Xiao, T. Xiong, H. Ang, X. Yuan, J.W. Chew, Visible-light-driven removal of tetracycline antibiotics and reclamation of hydrogen energy from natural water matrices and wastewater by polymeric carbon nitride foam, *Water Res.* 144 (2018) 215–225.
- [38] Z. Zhou, Z. Shen, C. Song, M. Li, H. Li, S. Zhan, Boosting the activation of molecular oxygen and the degradation of tetracycline over high loading Ag single atomic catalyst, *Water Res.* 201 (2021), 117314.
- [39] D. Wang, M.A. Mueses, J.A.C. Marquez, F. Machuca-Martinez, I. Grcic, R. Peralta Muniz Moreira, G. Li Puma, Engineering and modeling perspectives on photocatalytic reactors for water treatment, *Water Res.* 202 (2021), 117421.
- [40] I. Grcic, G. Li Puma, Photocatalytic degradation of water contaminants in multiple photoreactors and evaluation of reaction kinetic constants independent of photon absorption, irradiance, reactor geometry, and hydrodynamics, *Environ. Sci. Technol.* 47 (2013) 13702–13711.
- [41] R. Acosta-Herazo, M.A. Mueses, G.L. Puma, F. Machuca-Martinez, Impact of photocatalyst optical properties on the efficiency of solar photocatalytic reactors rationalized by the concepts of initial rate of photon absorption (IRPA)



- dimensionless boundary layer of photon absorption and apparent optical thickness, *Chem. Eng. J.* 356 (2019) 839–849.
- [42] I. Grčić, G. Li Puma, Six-flux absorption-scattering models for photocatalysis under wide-spectrum irradiation sources in annular and flat reactors using catalysts with different optical properties, *Appl. Catal. B: Environ.* 211 (2017) 222–234.
- [43] R. Peralta Muniz Moreira, G. Li Puma, Multiphysics computational fluid-dynamics (CFD) modeling of annular photocatalytic reactors by the discrete ordinates method (DOM) and the six-flux model (SFM) and evaluation of the contaminant intrinsic kinetics constants, *Catal. Today* 361 (2021) 77–84.
- [44] R. Acosta-Herazo, J. Monterroza-Romero, M.Á. Mueses, F. Machuca-Martínez, G. Li Puma, Coupling the six flux absorption-scattering model to the Henyey–Greenstein scattering phase function: evaluation and optimization of radiation absorption in solar heterogeneous photoreactors, *Chem. Eng. J.* 302 (2016) 86–96.
- [45] J. Liang, Q. Song, J. Wu, Q. Lei, J. Li, W. Zhang, Z. Huang, T. Kang, H. Xu, P. Wang, X. Zhou, P.K. Wong, H. Li, X. Meng, Z. Jiang, C.S. Lee, Anchoring copper single atoms on porous boron nitride nanofiber to boost selective reduction of nitroaromatics, *ACS Nano* 16 (2022) 4152–4161.
- [46] Y. Zhou, H. Qi, J. Wu, H. Huang, Y. Liu, Z. Kang, Amino modified carbon dots with electron sink effect increase interface charge transfer rate of Cu-based electrocatalyst to enhance the CO<sub>2</sub> conversion selectivity to C<sub>2</sub>H<sub>4</sub>, *Adv. Funct. Mater.* 32 (2022), 2113335.
- [47] J. Yang, X. Zhu, Q. Yu, M. He, W. Zhang, Z. Mo, J. Yuan, Y. She, H. Xu, H. Li, Multidimensional In<sub>2</sub>O<sub>3</sub>/In<sub>2</sub>S<sub>3</sub> heterojunction with lattice distortion for CO<sub>2</sub> photoconversion, *Chin. J. Catal.* 43 (2022) 1286–1294.
- [48] X. Ruan, X. Cui, Y. Cui, X. Fan, Z. Li, T. Xie, K. Ba, G. Jia, H. Zhang, L. Zhang, W. Zhang, X. Zhao, J. Leng, S. Jin, D.J. Singh, W. Zheng, Favorable energy band alignment of TiO<sub>2</sub> Anatase/Rutile heterophase homojunctions yields photocatalytic hydrogen evolution with quantum efficiency exceeding 45.6%, *Adv. Energy Mater.* 12 (2022), 2200298.
- [49] M. Zhong, X. Li, X. Chu, H. Gui, S. Zuo, C. Yao, Z. Li, Y. Chen, Solar driven catalytic conversion of cellulose biomass into lactic acid over copper reconstructed natural mineral, *Appl. Catal. B: Environ.* 317 (2022), 121718.
- [50] W. Weng, S. Wang, W. Xiao, X.W. Lou, Direct conversion of rice husks to nanostructured SiC/C for CO<sub>2</sub> photoreduction, *Adv. Mater.* 32 (2020), 2001560.
- [51] X. Ruan, X. Cui, G. Jia, J. Wu, J. Zhao, D.J. Singh, Y. Liu, H. Zhang, L. Zhang, W. Zheng, Intramolecular heterostructured carbon nitride with heptazine-triazine for enhanced photocatalytic hydrogen evolution, *Chem. Eng. J.* 428 (2022), 132579.
- [52] X. Ruan, C. Huang, H. Cheng, Z. Zhang, Y. Cui, Z. Li, T. Xie, K. Ba, H. Zhang, L. Zhang, X. Zhao, J. Leng, S. Jin, W. Zhang, W. Zheng, S.K. Ravi, Z. Jiang, X. Cui, J. Yu, A. Twin, S-scheme artificial photosynthetic system with self-assembled heterojunctions yields superior photocatalytic hydrogen evolution rate, *Adv. Mater.* (2022), e2209141.
- [53] C. Zhang, D. Qin, Y. Zhou, F. Qin, H. Wang, W. Wang, Y. Yang, G. Zeng, Dual optimization approach to Mo single atom dispersed g-C<sub>3</sub>N<sub>4</sub> photocatalyst: Morphology and defect evolution, *Appl. Catal. B: Environ.* 303 (2022), 120904.
- [54] R. Duan, S. Ma, S. Xu, B. Wang, M. He, G. Li, H. Fu, P. Zhao, Soybean straw biochar activating peroxydisulfate to simultaneously eliminate tetracycline and tetracycline resistance bacteria: Insights on the mechanism, *Water Res.* 218 (2022), 118489.
- [55] S. Ye, M. Cheng, G. Zeng, X. Tan, H. Wu, J. Liang, M. Shen, B. Song, J. Liu, H. Yang, Y. Zhang, Insights into catalytic removal and separation of attached metals from natural-aged microplastics by magnetic biochar activating oxidation process, *Water Res.* 179 (2020), 115876.
- [56] G. Huang, T.W. Ng, T. An, G. Li, D. Xia, H.Y. Yip, H. Zhao, P.K. Wong, Probing the intracellular organic matters released from the photocatalytic inactivation of bacteria using fractionation procedure and excitation-emission-matrix fluorescence, *Water Res.* 110 (2017) 270–280.
- [57] Y. Lin, X. Wu, Y. Han, C. Yang, Y. Ma, C. Du, Q. Teng, H. Liu, Y. Zhong, Spatial separation of photogenerated carriers and enhanced photocatalytic performance on Ag<sub>3</sub>PO<sub>4</sub> catalysts via coupling with PPy and MWCNTs, *Appl. Catal. B: Environ.* 258 (2019), 117969.